Astronomy & Astrophysics manuscript no. 15299
October 22, 2010

U-band study of the accretion properties in the σ Ori star-forming region ⋆

E. Rigliaco[1,2], A. Natta[1], S. Randich[1], L. Testi[1,3], and K. Biazzo[1]

[1] Osservatorio Astrofisico di Arcetri, INAF, Largo E.Fermi 5, I-50125 Firenze, Italy
[2] Università di Firenze, Dipartimento di Astronomia, Largo E.Fermi 2, I-50125 Firenze, Italy
[3] ESO, Karl-Schwarschild Strasse 2, D-85748 Garching bei München, Germany

Received 29 July 2010; accepted 9 October 2010

ABSTRACT

This paper presents the results of an U band survey with FORS1/VLT of a large area in the σ Ori star-forming region.We combine the U-band photometry with literature data to compute accretion luminosity and mass accretion rates from the U-band excess emission for all objects (187) detected by *Spitzer* in the FORS1 field and classified by Hernandez et al. (2007) as likely members of the cluster. The sample stars range in mass from $\sim$ 0.06 to $\sim$ 1.2 $M_\odot$; 72 of them show evidence of disks and we measure mass accretion rates $\dot{M}_{acc}$ between $< 10^{-11}$ and few 10^{-9} $M_\odot$/y, using the colors of the diskless stars as photospheric templates.Our results confirm the dependence of $\dot{M}_{acc}$ on the mass of the central object, which is stronger for low-mass stars and flattens out for masses larger than $\sim$ 0.3 $M_\odot$; the spread of $\dot{M}_{acc}$ for any value of the stellar mass is ∼2 orders of magnitude. We discuss the implications of these results in the context of disk evolution models. Finally, we analyze the relation between $\dot{M}_{acc}$ and the excess emission in the *Spitzer* bands, and find that at $\dot{M}_{acc} \sim 10^{-10}$ $M_\odot$/y the inner disks change from optically thin to optically thick.

Key words. Stars: formation - Accretion, accretion disks - open clusters and associations: individual: σ Orionis

1. Introduction

In recent years, our knowledge of the properties of young stars in several star-forming regions has made enormous progress. In particular, *Spitzer* observations have provided new information on the IR properties of circumstellar disks, and the discussion on how disks evolve in time has gained new momentum. In addition to the classical viscous evolution, which dissipates disks by accreting their matter onto the central stars, other processes such as gravitational instabilities, photoevaporation by X-ray and UV radiation of the central star (Hollenbach et al. 2000; Gorti & Hollenbach 2009), and planet formation (Dullemond et al. 2007) have been recognized to be important. Photoevaporation and planet formation may both shape the SED (spectral energy distribution) of so-called transitional disks, which have very low emission in the near- and mid-IR and strong excess emission at longer wavelengths (Calvet et al. 2002, 2005; D'alessio et al. 2006; Currie et al. 2009). In all cases, disks seem to come in all varieties: it is clear that neither time nor the mass of the system control them uniquely, and it seems very likely that disk properties and evolution depend also on the initial conditions, i.e., on the properties of the molecular core from which the star+disk system forms (Hartmann et al. 1998, 2006; Dullemond et al. 2006, Clarke 2007, Vorobyov & Basu 2009).

An important contribution to this discussion comes from measurements of the mass accretion rate for well characterized samples of stars. However, there are only few systematic determinations of the mass-accretion rates in large samples of objects within the same star-forming regions, covering a large range of central masses, with well measured SEDs and complete to include also diskless stars, limited so far to ρ-Oph (Natta et al. 2006) and Tr 37 (Sicilia-Aguilar et al. 2010).

In this paper, we add a third region, σ Ori, to the list. The σ Ori cluster is ideally suited for this kind of study. It contains more than 300 young stars, ranging in mass from the bright, massive multiple system σ Ori itself (the spectral type of the brightest star is O9.5V, Caballero. 2007) to brown dwarfs. It is located at a distance of $\sim$ 360 pc (*Hipparcos* distance 352^{+166}_{-85} pc for the O9.5V star Brown et al. 1994; Perryman et al. 1997) and has an age of $\sim$ 3Myr (Zapatero-Osorio et al. 2002; Oliveira et al. 2004). The region has negligible extinction (Bejar et al. 1999; Oliveira et al. 2004), and has been extensively studied in the optical, X-ray and infrared (e.g., Kenyon et al. 2005; Zapatero-Osorio et al. 2002; Jeffries et al. 2006; Franciosini et al. 2006; Hernandez et al. 2007; Caballero et al. 2007; Wolk 1996). Hernandez et al. (2007) have obtained *Spitzer* images of a large area in σ Ori in the four IRAC bands and with MIPS at 24 μm; they find 336 candidate members, of which 66% are class III stars and 34% show evidence of disks.

Accretion rates have been obtained by Gatti et al. (2008) for 35 objects in σ Ori from the luminosity of the near-IR hydrogen line Paγ; they found mass accretion rates lower on average than in younger regions. However, their sample was small and limited in mass (0.12–0.5 $M_\odot$). In this paper, we present the results for a much larger and better characterized sample from Hernandez et al. (2007). We measure mass accretion rates from the U-band excess emission, which originates in the accretion shock where accreting matter impacts on the stellar surface (Gullbring et al. 1998; Calvet & Gullbring 1998). The correlation between the U-band excess luminosity and the accretion luminosity has been established both empirically (Gullbring et al. 1998; Herczeg & Hillenbrand 2008) and theoretically (Calvet & Gullbring 1998). The U-band excess is an excellent proxy of

Send offprint requests to: erigliaco@arcetri.astro.it

⋆ Based on observations collected at the European Southern Observatory, Chile. Program 082.C-0313(A).

the accretion luminosity, which allows obtaining reliable values of the mass accretion rate for large samples of stars using little observing time when, as in σ Ori, the extinction is negligible. It very well complements measurements obtained from other tracers, such as the IR hydrogen recombination line luminosities (see the discussion in Herczeg & Hillenbrand 2008).

The paper is organized as follows: observations and data reduction are described in Sect. 2, the properties of the sample are derived in Sect. 3, in Sect. 4 we discuss the method used to derive the accretion properties. The results are discussed in Sect. 5 and 6. Three appendices present additional material on: the recomputation of accretion rates in ρ-Oph with the new distance and evolutionary tracks; the accretion properties of BD candidates beyond the Spitzer sample; and the properties of transitional and evolved disks in our sample.

2. Observations and data analysis

2.1. U-band photometry

We have performed a U-band survey that covers a total field of ~1000 arcmin^2 in the σ Orionis cluster. Observations were carried out with FORS1 mounted on the UT2 telescope at the VLT using u_HIGH filter and were performed in service mode during seven nights from October 2008 to March 2009. All the nights were photometric, with seeing in the range 0.6-1.5". We observed 28 fields (FOV 6'.8 × 6'.8) in σ Ori with an exposure time of 900 seconds each. The distribution of the pointings obtained with FORS1 is shown in Figure 1 and the log of the observation is provided in Table 1. The long exposure time on each field allowed us to reach a U-band limiting magnitude of ~23; objects brighter than U~17 mag are saturated. The fields around the two brightest stars of the quintuplet system containing σ Ori (within 0.2 pc projected distance) had to be excluded because of to light contamination.

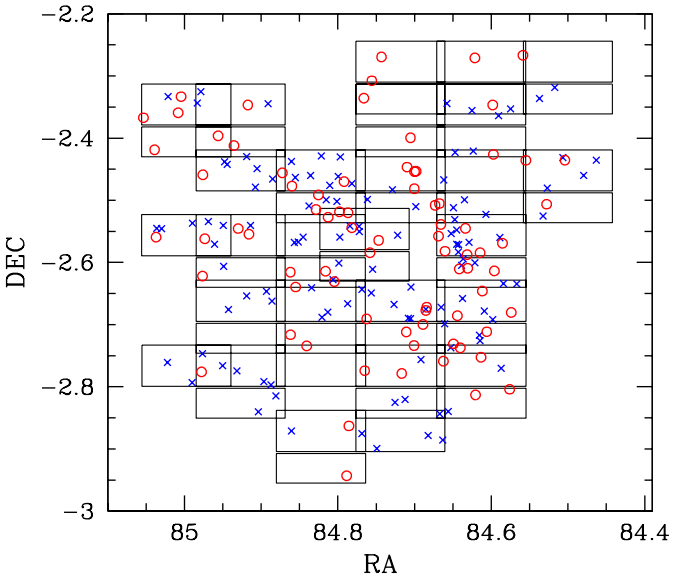

Fig. 1. Fields in the σ Ori cluster that have been imaged with FORS1 (solid boxes). Crosses show class III stars (blue in the online version of the figure), circles class II, TD and EV object (red in the online version of the figure), as classified by Hernandez et al. (2007).

Table 1. Journal of observations. RA and DEC refer to the pointing center.

Run dates (y-m-d)	Observed field	RA (○)	DEC (○)	Seeing (")
2008-10-05	field 1	84.5001	-2.30238	0.92
	field 3	84.7184	-2.30234	1.33
2008-10-06	field 6	84.9268	-2.37146	1.20
	field 7	84.9976	-2.37146	1.32
	field 8	84.5002	-2.47742	1.51
	field 10	84.7184	-2.47742	1.46
	field 11	84.8222	-2.47742	1.19
2008-10-08	field 13	84.6129	-2.58167	0.65
	field 15	84.8222	-2.58167	0.96
	field 16	84.9268	-2.58167	0.95
	filed 18	84.613	-2.68734	1.0
	field 19	84.7185	-2.68734	0.89
	field 20	84.8222	-2.68734	0.99
2008-12-21	field 2	84.613	-2.30234	0.81
	field 4	84.613	-2.37146	0.76
	field 5	84.7184	-2.37146	0.72
	field 9	84.6131	-2.47742	0.79
	field 22	84.613	-2.79169	0.74
	field 23	84.7184	-2.79169	1.09
	field 27	84.7184	-2.87086	0.73
	field 28	84.8221	-2.89632	0.68
2009-01-24	field 12	84.9267	-2.45196	0.95
	field 21	84.9267	-2.68734	0.96
	field 24	84.8221	-2.76621	1.06
2009-01-30	field 17	84.9976	-2.55619	0.99
	field 26	84.9974	-2.76621	0.78
2009-03-25	field 14	84.7653	-2.57167	0.70
	field 25	84.9268	-2.79169	0.69

2.2. Data reduction

The data were reduced using standard procedures including bias subtraction and flat fielding within the IRAF [1] package. We performed aperture photometry with the PHOT task in the APPHOT package, and using noao.digiphot.daophot routines for the photometry extraction. The stellar density was generally low enough to make aperture photometry acceptable. The IRAF routine MKAPFILE was used to determine and apply aperture corrections based on ensemble averages of stars in each separate frame. Astrometry correction was done to center the telescope coordinates. Photometric standard stars from Landolt (1992) and Persson et al. (1998) were observed at least once during each night and were used to flux-calibrate the images using the task PHOTCAL and to set the zero point magnitudes of each observing night and for both chips. Aperture photometry was performed using ten different apertures per image (0.5, 0.6, 0.7, 0.8, 0.9, 1.0, 1.25, 1.5, 2.0, 3.0 times the average FWHM). The inner radius of the sky annulus, which allowed us to define the sky brightness, was 10 times the average FWHM, while the width of the annulus was fixed at 10 pixels.

The uncertainties on the U-band magnitudes obtained are on the order of ±0.1 mag. They are dominated by systematic errors, the biggest of which is the error on the zero point magnitude (about 0.08 mag), which affects all measurements in the same manner; a second systematic term, on the order of 0.01 mag, is due to the color term correction with respect to the

[1] IRAF is distributed by National Optical Astronomy Observatories, which are operated by the Association of Universities for Research in Astronomy, Inc., under cooperative agreement with the National Science Foundation.

u_HIGH filter. Random errors owing to the aperture photometry technique used to derive the stellar flux and the sky brightness are also very small.

2.3. U-band variability

Young pre-main sequence stars are known to be variable, with timescale from hours to several days (e.g., Gomez de Castro et al. 1998; Hillenbrand et al. 1998; Briceño et al. 2001; Sicilia-Aguilar et al. 2005a, 2005b). The U-band variability is probably related to variations of the accretion rate, and, although a proper study is well outside the scope of this paper, it is interesting to estimate how large an effect this is likely to be.

In our FORS1 data there are 30 objects that lie at the superposition of two different fields and have therefore been observed twice, with separations that range between few days and few months. Of these, 19 are Class III stars and show no variability within the photometric uncertainty. Of the 11 Class II objects, 5 show no variability, 5 have variations between 0.15 and 0.4 mag, and one (SO866) has two measurements which differ by about 0.8 mag. This is similar to what is observed in other star-forming regions (see, e.g., Sicilia-Aguilar et al. 2010 and references therein).

Variability on a much longer time base can be checked by comparing our sample to that observed by Wolk (1996), where the observations were carried out in January 1996 with the 1 meter telescope CTIO. The two samples have ~30 class II stars in common (see Fig. 2). The comparison between the U band magnitude determinations shows a ΔU variation of at most 0.5 magnitudes, not different from what we observe on a shorter timescale.

A difference of 0.5 mag in the measured U-band magnitude corresponds to a L_{acc} and $\dot{M}_{acc}$ difference of a factor of at most two (see §4). This can be important when discussing individual objects. However, if the accretion properties of a large sample of stars are considered, it can only cause a moderate spread in the accretion values.

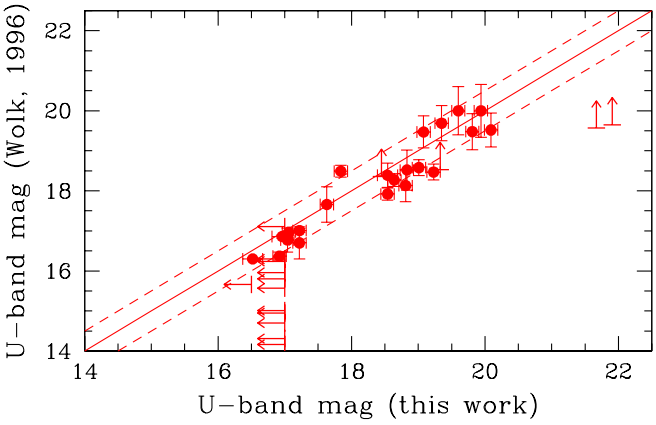

Fig. 2. U-band magnitude from Wolk (1966) and this work. Dashed lines correspond to an interval of ±0.5 mag.

2.4. Spectroscopy

Among the objects observed with FORS1, six have also optical spectroscopy obtained with SARG@TNG. We obtained spectroscopic observations in 2009 at the *Telescopio Nazionale Galileo* (TNG) during three nights from 27 to 29 January. The SARG spectrograph attached to the 3.58m telescope was used with the 2048×4096 CCD detector (pixel size = 13.5 μm) and the Yellow Grism CD#3 as cross-disperser. This allowed us to cover ~6200-8000 Å wavelength range. We used the slit #1 obtaining R =29 000 as spectral resolution.

The data reduction was performed by using the ECHELLE task of the IRAF package following the standard steps of background subtraction, division by a flat-field spectrum given by a halogen lamp, wavelength calibration using emission lines of a Thorium-Argon lamp, and sky subtraction.

With exposure times of 10-30 minutes we achieved signal-to-noise ratios (S/N) in the range 10–15 in the lithium line λ6708 region, depending on airmass and sky conditions. Each star was observed 1-3 times. All the spectra acquired per star were shifted in wavelength for the heliocentric correction and then co-added obtaining a S/N ratio in the continuum around 20.

3. The observed sample

Table C.2 gives the measured U-band magnitude of all the objects in the FORS fields listed as σ Ori members by Hernandez et al. (2007) based on optical and near-IR photometry. This sample of 187 objects (out of 336 members) is our basic sample and will be discussed below.

The Hernandez et al. (2007) sample spans the mass range from ~ 0.06 to 2–3 $M_\odot$, and is practically complete above 0.1 $M_\odot$. Based on the SED in the IRAC spectral range (from 3.6 μm to 8.0 μm) the *Spitzer* sources are divided in in class II stars, pre-main sequence stars with IR excess typical of optically thick disks (classical TTauri stars CTTs or CII), class III stars, with typical colors of stellar photospheres (weak-line TTauri stars WTTs or CIII), and stars with non-classical disks, in turns divided in "evolved disks" (EV), with small excess emission at all infrared wavelengths, and "transitional disks" (TD), which have zero or very low emission in the near infrared but normal excess at longer wavelengths. Below we will refer to class II, TD, and EV objects as "disk objects".

Our sample includes 115 class III members, and 72 objects with evidence of disks. Among these, there are 54 class II stars, 4 TD (out of the 7 possibly identified by Hernandez et al. 2007), and 14 EV disks. Of the 72 stars with disks, 54 are detected in the U-band, 6 are non-detections, and 12 are saturated. Out of the 115 class III stars, 83 are detected, 7 are not, and 25 are saturated.

The spatial distribution of the observed sample is shown in Fig. 1.

3.1. Stellar properties

Spectroscopically determined spectral types exist for a small fraction of the σ Ori objects only (Zapatero-Osorio et al. 2002; Barrado y Navascues et al. 2003; Muzerolle et al. 2003). Therefore, we determine the stellar parameters (effective temperature, luminosity, mass, and radius) of all objects in a homogeneous way from multi-color photometry.

Table C.2 reports for each object broad-band magnitudes collected from the literature. The optical photometry is from Sherry et al. (2004); Zapatero-Osorio et al. (2002); Kenyon et al. (2005); Béjar et al. (2001) and Wolk (1996). The JHK magnitudes are

taken from the Two Micron All Sky Survey (2MASS) (Cutri et al. 2003). The magnitudes in the four channels of the Infrared Array Camera (IRAC; 3.8-8.0 μm) and the first channel of the Multiband Imaging Photometer for *Spitzer* (MIPS; 24 μm) are from Hernandez et al. (2007). When two or more magnitude determinations for the same band were available, we choose, if possible, measurements obtained by the same author.

We derived the effective temperatures of each star by comparing the observed magnitudes to the synthetic colors computed from the model atmosphere of Baraffe et al. (1998) for $\log g$=4.0 and the appropriate filter passband and zero fluxes. Luminosities were then computed using the I-band magnitude and the bolometric correction for ZAMS stars and the T_{eff} – spectral type correlation of Kenyon & Hartmann (1995) and Luhman et al. (2003). We assumed a distance of D=360 pc, and negligible extinction in all bands (Brown et al. 1994; Bejar et al. 1999).

We performed two checks on the T_{eff} estimates. In a first test, we compared the values derived from the model atmosphere synthetic colors with those obtained by comparing the observed colors (V-R), (V-I) and (R-I) to those of ZAMS stars. The differences are within 150 K for 90% of the stars, with a slight systematic tendency toward higher values for model atmosphere estimates. A second test is given by the comparison of our estimates of T_{eff} with the spectroscopic determination derived from low- and medium-resolution observations. In a sample of 22 objects in the range ~ 3200–4000 K we find differences of ±150 K at most.

The distribution of the stars in the HR diagram is shown in Fig. 3 with the evolutionary tracks and isochrones from Baraffe et al. (1998). The sample covers the mass range between ~1.2 to ~0.05 $M_\odot$; both the lower and the higher mass limit reflect the sensitivity limit of the *Spitzer* survey (see discussion in Hernandez et al. 2007). The median age is about 3 My, with a rather large spread, which is similar for Class II and Class III objects. This spread also remains when only radial velocity confirmed members are considered (Sacco et al. 2008; Kenyon et al. 2005). The issue of the spread in age in σ Ori as well as in other young star-forming regions has been discussed in several papers (e.g. Hillenbrand 2009 and references therein) and further discussion is beyond the purpose of this paper. Note, however, that the error bars may be quite large and affect the age estimates significantly.

The stellar parameters of all Class II objects are summarized in Table 2.

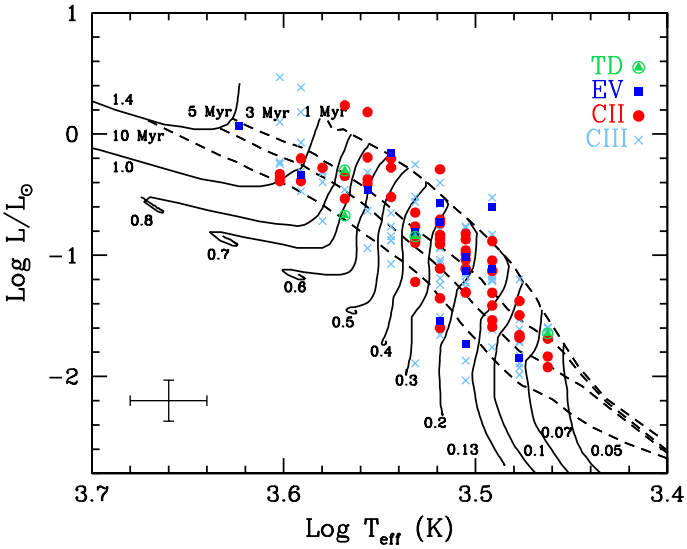

Fig. 3. Location of the observed objects (class III, class II, and objects with "non-classical" disks, as labeled) on the HR diagram. Evolutionary tracks and isochrones are taken from Baraffe et al. (1998). Stellar masses and ages are labeled. The horizontal bar refers to the error on the effective temperature, the vertical bar reflects the error of the bolometric correction of the ZAMS stars related to the error on the effective temperatures.

4. Mass accretion rate

Matter accreting from the disk onto the star, channeled along field lines, shocks at the stellar surface. About half of the accretion luminosity is released with a typical color temperature of ~ 10^4 K, i.e., much hotter than the stellar photosphere (Hartigan et al., 1991, Gullbring & Calvet, 1998). The resulting excess emission is clearly detected at short wavelengths, in the U-band in particular. It has been shown (Gullbring & Calvet 1998, Herczeg & Hillendrand 2008) that the U-band excess luminosity is an accurate proxy of the accretion luminosity, which can be reliably used to measure L_{acc} for T Tauri stars and BDs.

4.1. Class III sources

In order to measure the excess of luminosity in U-band for a given object, we need to know the measured U-band luminosity and the expected photospheric U band luminosity for a non-accreting star with the same parameters. This is not trivial, as young stars tend to have a significant level of chromospheric activity that causes continuum emission at short wavelengths; this is not related to accretion and must, therefore, be counted as "photospheric" contribution for our purpose.

We take advantage of the large number of Class III stars in our sample to define the typical colors of non-accreting young stars. Fig. 4 plots the class III (U-J), (U-I), (U-R) and (U-V) colors as a function of the effective temperature of the star. For each color index, there is a tight correlation with the effective temperature; the solid lines show the best fits, the dashed lines the 2σ errors, which are ~ 0.5 mag at most. Hereafter, we will refer to the ±2σ as the photospheric strip. Note that while (U-J) increases with T_{eff}, (U-V) slightly decreases.

4.2. Disk sources

To derive the U-band excess emission in class II objects we assign to each of them the photospheric colors of class III stars of the same T_{eff}, according to the correlations shown in Fig. 4; we assume that there is negligible excess emission in the V, R, I, and J band and derive the U-band excess from the difference between the observed and the photospheric colors. We use (U-I), as I-band magnitudes are available for all stars in our sample (see Table C.2), using the relation:

$$\Delta U_{excess} = (U-I)_{obs} - (U-I)_{phot}, \quad (1)$$

where $(U-I)_{obs}$ are the observed (U – I) color, and $(U-I)_{phot}$ is the assigned photospheric color.

We define as accreting all stars with ΔU_{excess} larger than the 2σ uncertainties of the photospheric colors, as derived in §4.1. Class II stars with colors within the class III photospheric strip will be considered not-accretors and we can only assign upper limits to the accretion luminosity and mass accretion rate.

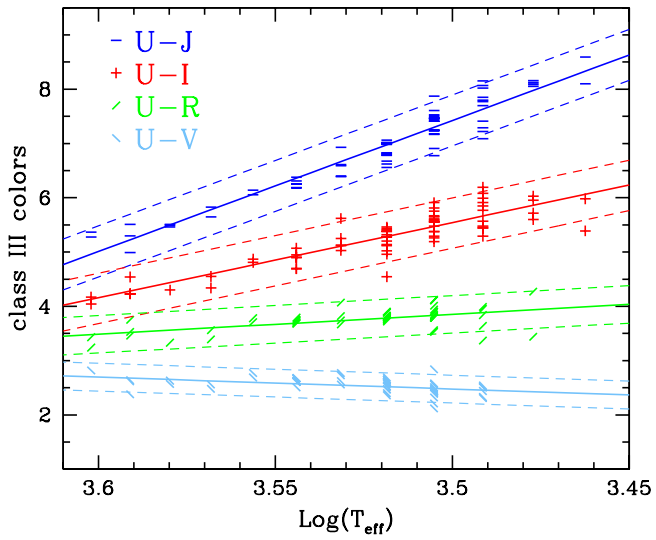

Fig. 4. Colors of Class III stars vs. effective temperature. Blue horizontal lines plot (U-J), red crosses (U-I), green 45deg lines (U-R), cyan -45deg lines (U-V), as labeled. The solid lines show the best fit, the dashed lines $\pm 2\sigma$. In the text, we will define the region between the dashed lines as the photospheric strip. (A color version of this figure is available in the online journal.)

We choose the 2σ uncertainty as good compromise not to loose low-accreting stars. After defining the accreting or non-accreting stars, we computed the excess flux in the U-band as:

$$F_{U,exc} = F_{0,U} \times \left(10^{-U_{obs}/2.5} - 10^{-((U-I)_{phot}+I_{obs})/2.5}\right), \quad (2)$$

where $F_{0,U}$ is the zero point flux in the U-band.

Figure 5 shows the comparison between the accretion luminosities computed from (U-I) vs those derived from (U-J), (U-R) and (U-V), respectively, for all objects with available photometry. The derived L_{acc} are the same within a factor $\sim$ 3 for all objects, and for 70% of them the agreement is within a factor 1.5. These results support several aspects of our procedure: within the above uncertainties: firstly, our assumption that reddening is negligible at all wavelengths; secondly, that there is negligible excess emission in V, R, I, and J; thirdly, since the photometric data are collected from the literature and are not simultaneous, that variability is not the major limiting factor in deriving the accretion properties (although it may introduce some scatter in the measurements).
We use the (U-I) color to define the accretion rates. Assuming an uncertainties in U-band of 0.5 mag we estimate an error on the U-band luminosities of a factor 3 at most.

4.3. Accretion rate

The U-band luminosity obtained from the excess flux in the U-band (Eq. 2) is converted into total accretion luminosity L_{acc}, which is roughly the amount of energy released by gas that accretes onto the star, using the approximately linear relation derived for T Tauri stars (Gullbring & Calvet 1998) and brown dwarfs (Calvet & Gullbring 1998; Herczeg & Hillendrand 2008):

$$\log\left(\frac{L_{acc}}{L_\odot}\right) = \log\left(\frac{L_U}{L_\odot}\right) + 1.0. \quad (3)$$

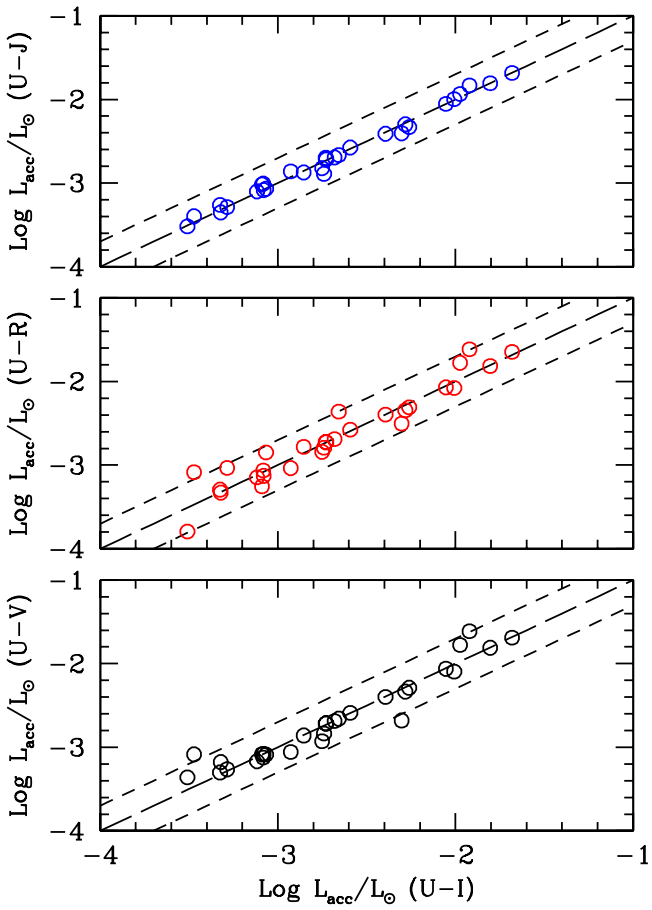

Fig. 5. Values of the accretion luminosity derived from (U-J), (U-R), (U-V) vs. the value derived from (U-I), as described in the text for a sub-sample of 30 objects. The dashed lines correspond to ± 0.5 in $\log L_{acc}$.

Knowing M_*, R_* and the accretion luminosity L_{acc} we derive the mass accretion rate $\dot{M}_{acc}$ with the relation

$$\dot{M}_{acc} = \left(1 - \frac{R_*}{R_{in}}\right)^{-1} \frac{L_{acc}\, R_*}{G\, M_*} \sim 1.25 \frac{L_{acc}\, R_*}{G\, M_*}, \quad (4)$$

where G is the universal gravitational constant and the factor $(1 - \frac{R_*}{R_{in}})^{-1} \sim 1.25$ is estimated by assuming that the accretion gas falls onto the star from the truncation radius of the disk (R_{in} $\sim 5R_*$; Gullbring et al. 1998).

Table 2 reports 72 actual values of $\dot{M}_{acc}$. Thirty stars have $\dot{M}_{acc}$ detection. In 30 cases, we can only estimate upper limits to $\dot{M}_{acc}$. Of these, 6 are objects with U-band emission below our detection limit, while 24 have colors within the photospheric strip (§4.2). Eight stars have expected U-band photospheric emission brighter than our saturation limit (labeled "sat"), and 4 stars have U < 17 mag, but colors with a lower limit than $\dot{M}_{acc}$ can be safely estimated because their photospheric contribution is lower than the saturation limit, and the upper limit in the U-band can be only due to the accretion process.

The lowest values of $\dot{M}_{acc}$ we can estimate range from $\sim 10^{-11}$ $M_\odot$/y for very low, cold objects to few 10^{-10} $M_\odot$/y for solar-mass stars. This trend occurs because the minimum detectable value of $\dot{M}_{acc}$ from U-band photometry depends not only on the depth of the photometry, but also on the physical

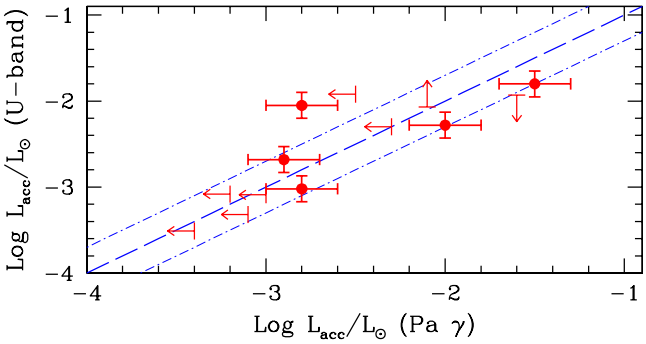

Fig. 6. Comparison between L_{acc} computed from Paγ (Gatti et al. 2008) and L_{acc} obtained from U-band photometry for stars in common. The dashed line refers to the same value of L_{acc} , the dashed-dotted lines to ±0.5 in log L_{acc}.

properties of the star, and on how well one can estimate the photospheric flux. Indeed, this is at present the major limiting factor.

The uncertainties on individual measurements of L_{acc} and $\dot{M}_{acc}$ are quite large. They come from the combination of photometric errors and variability, the definition of the class III colors, the adopted relation between the U-band excess luminosity and the accretion luminosity, and between the latter and $\dot{M}_{acc}$ and the uncertainty on the value of R_*/M_*(see also Sicilia-Aguilar et al. 2010). Some of these uncertainties have been discussed in the previous sections, while others, e.g., the differences owing to different evolutionary tracks, by other authors (Fang et al. 2009). Our estimate is that in general $\dot{M}_{acc}$ is known with an uncertainty of a factor 3–5.

5. Results

Detectable values of accretion luminosity and mass accretion rate were obtained for 42% of disk objects. Another 42% have upper limits in accretion luminosity and mass accretion rate. The remaining 16% have lower limits (see §4.3).

Gatti et al. (2008) compute L_{acc} from the luminosity of the hydrogen recombination line Paγ, following the procedure described by Natta et al. (2006).

Figure 6 compares the values of L_{acc} derived with the two different methods (U-band excess emission and Paγ recombination line respectively) for the 12 stars we have in common; it agrees well. Another nine stars of the Gatti et al. (2008) sample are class II objects and were observed with *Spitzer*. We could not observe these stars either because they are outside the FORS fields, or because they are close to the brighter stars of the σ Ori quintuplet system. We added these nine stars to our sample. In Table. 3 the properties of the sub-sample derived from Gatti et al. (2008) are listed. For these stars we recomputed the stellar properties adopting the Baraffe et al. (1998) evolutionary tracks., in the same way as for the present sample.

Figures 7 - 10 show the relations between the accretion properties and different physical and morphological properties of the observed sample.

In Fig. 7 we specifically plot the accretion luminosity as a function of the stellar luminosity for all class II objects; transitional and evolved disks are shown by different symbols. The figure shows that very few stars have L_{acc} larger than 0.1 L_{star}, and that most of them have values well below this limit.

Table 2. Accretion properties of the class II objects and objects with transitional and evolved disks.

Object	class	M_* ($M_\odot$)	L_* ($L_\odot$)	T_{eff} (K)	logL_{acc} ($L_\odot$)	logM_{acc} ($M_\odot$ yr^{-1})
SO299	TD	0.35	0.14	3400	-2.93	-9.82
SO341	II	0.60	0.39	3600	< -2.26	< -9.32
SO397	II	0.30	0.18	3300	-2.73	-9.48
SO435	II	0.20	0.09	3200	< -3.38	< -10.07
SO444	EV	0.35	0.16	3400	< -2.90	< -9.78
SO462	II	0.20	0.15	3200	-3.08	-9.67
SO482	II	0.20	0.05	3200	-3.08	-9.91
SO485	II	0.25	0.04	3300	-2.39	-9.37
SO490	II	0.15	0.07	3100	-2.73	-9.32
SO500	II	0.10	0.02	3000	-3.27	-9.92
SO514	II	0.13	0.04	3100	< -3.88	< -10.56
SO518	II	1.00	0.41	4000	sat	sat
SO520	II	0.30	0.15	3300	< -3.02	< -9.82
SO537	II	0.07	0.02	3000	< -4.32	< -10.83
SO540	II	1.00	0.43	4000	sat	sat
SO562	II	0.40	0.22	3400	-1.80	-8.66
SO563	II	0.40	0.51	3300	-2.30	-8.95
SO583	II	0.75	1.52	3600	sat	sat
SO587	EV	0.30	0.27	3300	< -2.78	< -9.45
SO598	II	0.20	0.11	3200	-3.09	-9.75
SO615	EV	0.60	0.69	3500	sat	sat
SO638	EV	1.00	0.46	3900	sat	sat
SO646	II	0.30	0.12	3300	-2.05	-8.89
SO657	II	0.06	0.02	2900	< -4.49	< -10.91
SO662	II	0.90	0.41	3900	< -2.06	< -9.26
SO663	II	0.20	0.14	3200	< -3.20	< -9.82
SO674	II	0.30	0.14	3300	< -3.06	< -9.88
SO697	II	0.60	0.63	3500	-1.92	-8.76
SO700	EV	0.08	0.01	3000	< -4.46	< -11.11
SO710	II	0.50	0.30	3500	-2.28	-9.19
SO728	EV	0.20	0.25	3100	< -3.08	< -9.53
SO736	II	0.80	1.73	3700	sat	sat
SO738	II	0.11	0.03	3100	< -4.04	< -10.7
SO739	II	0.10	0.04	3000	< -4.03	< -10.54
SO750	II	0.09	0.03	3000	-3.51	-10.03
SO759	EV	0.30	0.19	3300	< -2.97	< -9.67
SO762	II	0.13	0.05	3100	< -3.82	< -10.44
SO774	II	1.00	0.47	4000	< -1.93	< -9.17
SO818	TD	0.70	0.21	3700	-2.26	-9.45
SO827	II	0.35	0.06	3400	-2.74	-9.82
SO844	II	0.60	0.42	3600	-2.01	-8.95
SO848	II	0.20	0.03	3300	-2.85	-9.86
SO859	II	0.35	0.17	3400	-2.75	-9.61
SO865	II	0.35	0.13	3400	-2.59	-9.50
SO866	II	0.20	0.05	3200	-3.28	-10.12
SO897	TD	0.80	0.50	3700	> -2.07	> -9.13
SO905	EV	0.60	0.35	3600	< -2.39	< -9.38
SO908	EV	0.20	0.10	3200	-2.68	-9.37
SO917	EV	0.20	0.03	3300	< -3.73	< -10.71
SO927	II	0.70	0.29	3700	< -2.41	< -9.53
SO936	II	0.08	0.01	2900	< -4.58	< -11.19
SO967	II	0.25	0.08	3300	< -3.39	< -10.25
SO981	EV	1.3	1.17	4200	sat	sat
SO984	II	0.90	0.53	3800	< -2.12	< -9.24
SO1009	EV	0.15	0.02	3200	-1.97	-8.89
SO1036	II	0.75	0.45	3700	< -2.17	< -9.22
SO1050	II	0.20	0.08	3200	< -3.49	< -10.22
SO1057	EV	0.15	0.08	3100	< -3.67	< -10.25
SO1059	II	0.06	0.01	2900	< -4.33	< -10.86
SO1075	II	0.17	0.13	3100	> -1.66	> -8.18
SO1156	II	1.00	0.63	3900	sat	sat
SO1182	II	0.20	0.10	3200	-3.12	-9.79
SO1193	II	0.11	0.03	3100	-3.32	-10.01
SO1230	II	0.20	0.08	3200	-3.32	-10.06
SO1260	II	0.35	0.13	3400	-1.68	-8.60
SO1266	II	0.16	0.07	3100	-3.47	-10.09
SO1268	TD	0.09	0.02	2900	< -4.49	< -11.06
SO1274	II	0.70	0.64	3600	> -2.15	> -9.07
SO1323	EV	0.20	0.07	3200	< -3.51	< -10.25
SO1327	II	0.30	0.20	3300	-2.66	-9.39
SO1361	II	0.55	0.53	3500	> -1.82	> -8.65
SO1362	II	0.15	0.09	3100	-3.07	-9.61

Table 3. Accretion properties of the class II objects taken from Gatti et al. (2008). The masses and luminosities of the listed stars have been recomputed according the Baraffe et al. (1998) evolutionary tracks.

Object	class	M_* ($M_\odot$)	L_* ($L_\odot$)	T_{eff} (K)	logL_{acc} ($L_\odot$)	logM_{acc} ($M_\odot$ yr^{-1})
SO451	II	0.30	0.12	3350	-2.20	-9.10
SO682	II	0.60	0.30	3575	< -2.50	< -9.30
SO694	II	0.15	0.10	3075	< -3.20	< -9.80
SO723	II	0.25	0.10	3250	-2.00	-8.90
SO726	II	0.60	0.42	3575	-1.80	-8.60
SO733	II	0.45	0.36	3425	-2.00	-8.70
SO871	II	0.45	0.10	3500	< -3.20	< -10.30
SO1152	II	0.60	0.30	3575	< -2.40	< -9.30
SO1248	II	0.13	0.13	3000	< -2.80	< -9.30

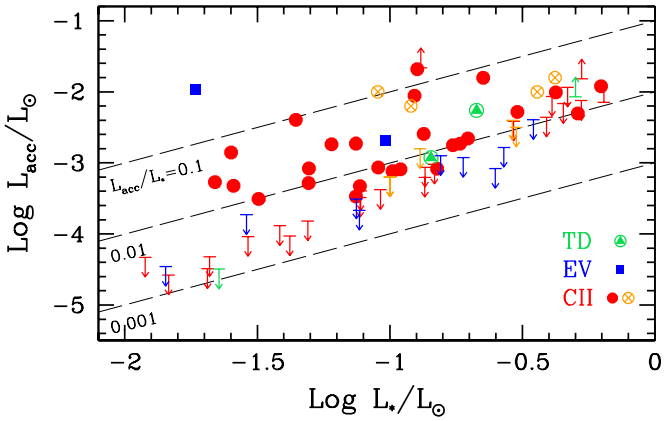

Fig. 7. Accretion luminosity as a function of the stellar luminosity for class II, EV, and TD disks, as labeled. The dashed lines show L_{acc}/L_{star} = 0.001, 0.01, and 0.1, respectively. The crosses surronded by a circle are the class II stars included here from the Gatti et al. (2008) sample, and listed in Table 3. Different colors for lower and upper limits can be distinguished in the online version of the journal.

The accretion luminosities for the detected sources range mainly from $\sim 10^{-2}L_\odot$ to $\sim 10^{-4}L_\odot$. For any given L_* there is a large range of measured L_{acc} that does not seem to vary significantly with L_* .

Figure 8 shows the mass accretion rate of class II stars as function of M_*. The data show a clear trend of increasing $\dot{M}_{acc}$ with increasing M_*. Including upper and lower limits as actual detections, we find $\dot{M}_{acc} \propto M_*^{1.6\pm0.4}$ with ASURV (Astronomy Survival Analysis Package, Feigelson & Nelson 1985). The trend is confirmed using two different methods (the EM algorithm and the BJ algorithm) within the ASURV package. The slope became flatter when we excluded the upper and lower limits in the analysis, but remained still within the uncertainties. From this plot we can clearly also see the large spread in $\dot{M}_{acc}$ (about two orders of magnitude) for any value of M_*.

In Fig 9 we plot the mass accretion rates versus the age of the stars.

Finally, in Fig 10 we plot the mass accretion rates as function of the projected distance from the central and bright O9.5 star σ Ori. We do not find any correlation between the mass accretion rates or the disk morphologies and the distance from σ Ori; it seems that the vicinity of the O9.5 star does not affect

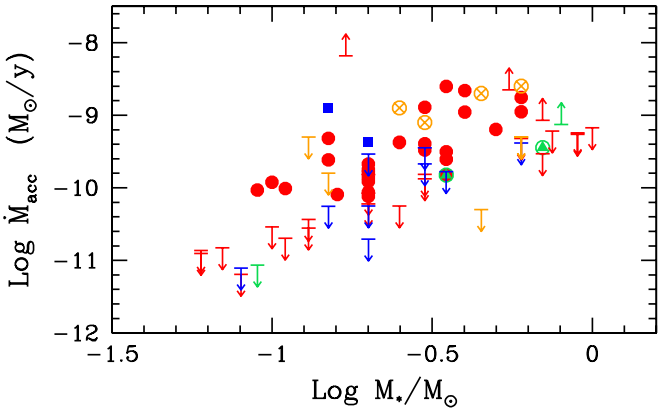

Fig. 8. Mass accretion rate as function of stellar mass. Symbols as in Fig. 7. (A color version of this figure is available in the online journal.)

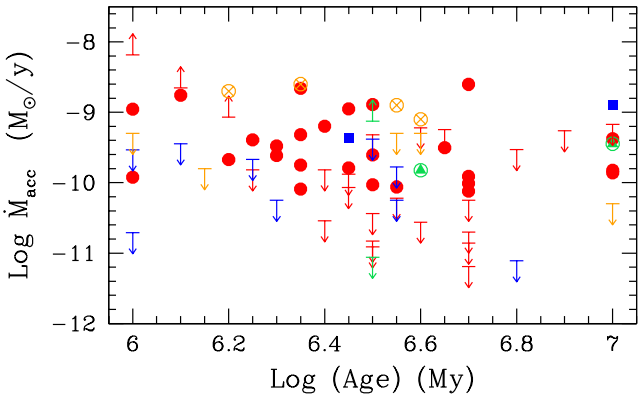

Fig. 9. Mass accretion rate as function of the age of the stars. Symbols as in Fig. 7.

the disk properties significantly (see also Hernandez et al. 2007). Rigliaco et al. (2009) studied in detail one object (SO587), which has a projected distance of 0.3 pc; based on literature U-band photometry and optical spectroscopy, they proposed that its disk is in the process of being photoevaporated, either by σ Ori or by its own central star. There are six additional objects with a projected distance of$\lesssim$0.3 pc from σ Ori with a $\dot{M}_{acc}$ range of more than a factor of ten, and it would be interesting to obtain high-resolution optical spectra to study wind diagnostics such as the optical forbidden lines of [SII], [NII] and [OI].

We caveat that in both Fig. 9 and Fig. 10 we did not divide stars in mass bins (which would result in too low number statistics); thus the relationship of $\dot{M}_{acc}$ vs. M_* seen in Fig. 8 might mask possible trends between $\dot{M}_{acc}$ and age or $\dot{M}_{acc}$ and the projected distance from σ Ori.

6. Discussion

6.1. $\dot{M}_{acc}$ as function of M_* and time

The distribution of mass accretion rates in a star-forming region traces the physical processes that control disk formation and evolution over the lifetime of the region, as well as the initial conditions, i.e., the mass and angular momentum distribution of the molecular cores from which the stars form. It is a snapshot in

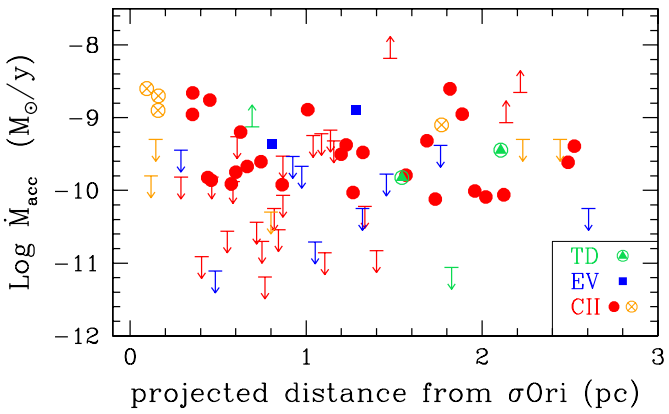

Fig. 10. Mass accretion rates versus projected distance from the bright stars σ Ori in parsec. (A color version of this figure is available in the online journal.)

time, which needs to be compared to models that follow disk formation and evolution up to the age of the region (e.g., Dullemond et al. 2006; Vorobyov & Basu 2008, 2009).

It has been known for some years that mass accretion rates increase on average with the mass of the central object. In σ Ori, a logarithmic linear correlation over the whole mass range, $\dot{M}_{acc} \propto M_*^{1.6\pm0.4}$ (Sec. 5), is similar within the uncertainties to what has found in Taurus (Calvet et al. 2004) and Ophiuchus (Natta et al. 2006), but flatter than in L1630N and L1641 (Fang et al. 2009). However, in σ Ori the trend seems to be flatter for higher mass stars than for lower mass objects, as also noted by Vorobyov & Basu (2008) in a compilation of all known $\dot{M}_{acc}$ values in various star-forming regions. This is shown in Fig. 11, which plots median values of $\dot{M}_{acc}$ as function of M_* for Class II and TD disks. All M_* intervals above 0.1 $M_\odot$ contain roughly the same number of stars (12–20). The values plotted in Fig. 11 treat upper and lower limits as actual detections; if we make the alternative assumption that lower (upper) limits are all smaller (larger) than the lowest (highest) measured value in the bin, the changes are very small; however, the large number of limits and the small number of objects in each bin make it meaningless to derive values for the upper and lower quartiles, to characterize the spread of $\dot{M}_{acc}$ seen in Fig.8. The mass interval below 0.1 $M_\odot$ contains only two detections and six upper limits to $\dot{M}_{acc}$, and the value in Fig. 11 (Log $\dot{M}_{acc}$=-10.8 $M_\odot$/y) should be considered as an upper limit to the median. The deficit of relatively strong accretors among the σ Ori BDs is confirmed by the analysis of a much larger (40 objects, see Appendix B), optically selected sample of very low-mass stars and BDs (Lodieu et al. 2009), included in our U-band survey, which contains only five objects with Log $\dot{M}_{acc}$> −10.8 $M_\odot$/y, two of which are also in the Hernandez et al. (2007) *Spitzer* sample.

The flattening of the $\dot{M}_{acc}$ vs. M_* relation at higher masses is very clear. Vorobyov & Basu (2009) compute numerical models of the collapse of a distribution of prestellar cores that include the formation and evolution of circumstellar disks and follow it for 3 My, roughly the age of σ Ori. Their models predict a flattening of the $\dot{M}_{acc}$ vs. M_* relation for stellar masses higher than about 0.3 $M_\odot$, due to the effect of gravitationally induced torques in the early stages of the evolution after the formation of the central star. These gravitational instabilities have little effect on lower-mass objects, where viscous evolution dominates at all times. Although the $\dot{M}_{acc}$ values predicted by Vorobyov & Basu (2009) are somewhat higher than the observations, the σ Ori results definitely support their models and the importance of self-gravity in the early evolution of more massive disks, already suggested by, e.g., Hartmann et al. (2006).

The Vorobyov & Basu (2009) models include only viscous evolution and gravitational instability; other physical processes may occur during σ Ori lifetime, such as photoevaporation and planet formation, leading to disk dissipation on shorter time scales. This may be a selective process, if, as indicated by the statistics of IR-excess emission for stars of different mass in different star-forming regions, disk dissipation occurs faster in more massive stars. In σ Ori, for example, Hernandez et al. (2007) estimate a fraction of objects with disks that increases from ∼ 10% for Herbig Ae/Be stars to ∼ 35% for T Tauri stars and BD candidates. If so, the comparison of the observations with the model predictions needs to be taken with care.

A way to investigate the relative importance of these different processes is to compare the statistical properties of the distribution of $\dot{M}_{acc}$ on M_* for regions of different age. This approach is limited at the moment because to the best of our knowledge, there are only two other suitable samples: ρ-Oph (Natta et al. 2006) and Tr 37 (Sicilia-Aguilar et al. 2010). In other cases, no mass accretion rates are available for complete sample of Class II objects (as in Taurus), or upper limits to $\dot{M}_{acc}$ are not provided (as in the two Orion regions studied by Fang et al. 2009), which makes statistical studies very difficult.

We have computed median values of $\dot{M}_{acc}$ in ρ-Oph from the results of Natta et al. (2006), which we revised to take into account the new estimates of the distance that were recently published (see Appendix A for details). The ρ-Oph sample covers a mass range between ∼ 0.03 and 3 $M_\odot$; the median values of $\dot{M}_{acc}$ are shown in Fig. 11; the figure also shows the results for the older (about 4 My), more distant region Trumpler 37, for which Sicilia-Aguilar et al. (2010) provide values of $\dot{M}_{acc}$ derived from U-band photometry for a *Spitzer*-selected sample of stars. The stars cover the mass range 0.4-1.6 $M_\odot$, based on the Siess et al. (2000) evolutionary tracks.

For M_* roughly larger than 0.2 $M_\odot$, the three regions have similar values of the median $\dot{M}_{acc}$ within the uncertainties in spite of their difference in age (more than a factor of 3). If the disk properties at a very early stage were the same, this would imply a slower time evolution of $\dot{M}_{acc}$ than predicted by disk models (see, e.g., Hartmann et al. 1998; Dullemond et al. 2006; Vorobyov & Basu 2009) and confirms the result of Sicilia-Aguilar et al. (2010), based on a small sample of stars for which individual ages could be estimated. The difference between $\dot{M}_{acc}$ medians increases as M_* decreases, and becomes very large (factor of 10 at least) for $M_* < 0.1$ M_* between ρ-Oph and σ Ori. This is consistent with the predictions of viscous models if the original disk properties in the two regions are the same and no disk around these very low-mass stars dissipates within, e.g., 3 My.

If indeed the apparent slow time evolution of solar mass stars is a result of the continuous loss of the less massive, for the lower accreting disks the two different effects (namely the decrease of $\dot{M}_{acc}$ with time, and dissipation of disks once they fall below a critical $\dot{M}_{acc}$ value) roughly compensate, so that median $\dot{M}_{acc}$ changes little. If that is true, one should find that the lowest values of $\dot{M}_{acc}$ do not vary with time, because they are fixed by disk dissipation, while the highest values decrease as expected from viscous evolution. There is a hint that this is indeed the case (seel also L1641 and L1630; Fang et al. 2009), but the statistics is poor and the definition of the upper envelope to the $\dot{M}_{acc}$ values too uncertain for the moment.

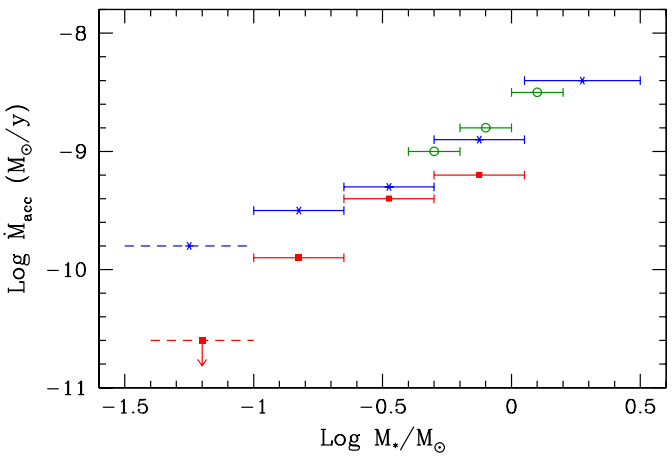

Fig. 11. Median values of $\dot{M}_{acc}$ as function of M_*. Red lines (with a central square) refer to σ Ori Class II and TD disks; the lowest mass bin should be considered as an upper limit only (see text). Blue lines (crosses) show the distribution for ρ-Oph (data from Natta et al. 2006, see Appendix A); green lines (circles) for Tr 37 (data from Sicilia-Aguilar et al. 2010). (A color version of this figure is available in the online journal.)

6.2. Mass accretion rates vs disks morphologies

Fig. 12 plots the mass accretion rates for the σ Ori sample as function of the excess over the photospheric emission for the four IRAC bands and for the 24 μm MIPS band. The excess emission is defined as the difference between the observed (*Spitzer*-I) color and that of Class III stars of the same effective temperature, assuming that no excess is present in the I band. In each panel, the horizontal bars show the median of the excess distribution for Class II disks and the lower and upper first quartile; for comparison, we also show the lower and upper first quartile of the excess for the Taurus median SED of classical disks (D'Alessio et al. 2006).

The median of the excess emission distributions is lower in σ Ori than in Taurus, as expected if on average σ Ori stars are older than Taurus objects, suggesting a higher degree of grain settling in older regions (e.g., Hernandez et al. 2007). Note that the σ Ori sample includes lower-mass objects than the Taurus one, and that disk models predict lower excess fluxes for BDs in this range of wavelengths; however, we do not find any correlation of the measured excess with the mass of the star, and we tend to exclude that the difference between the two regions is due to the different mass range only. The figure also shows the location of the 11 EV disks with a determination of $\dot{M}_{acc}$ and the 4 TD; for six of them we also show complete SEDs and Hα profiles in Appendix C.

There is no statistically significant correlation of $\dot{M}_{acc}$ with the excess emission. However, there are a few aspects of these plots that can be understood if, as expected in viscous models, $\dot{M}_{acc}$ traces the surface density of the inner disk. Objects with $\dot{M}_{acc}\sim 10^{-10} - 10^{-9}$ M$_\odot$/y are distributed over the whole range of excess values. This is expected in optically thick disks, where the observed emission depends on inclination, inner radius and degree of flaring, but not on the actual disk surface density. Objects with $\dot{M}_{acc}\lesssim 10^{-10}$ M$_\odot$/y tend to have very low excess in all *Spitzer* bands. We think that most of them have in fact optically thin disks, which are characterized by much lower emission, roughly proportional to the surface density, i.e., to $\dot{M}_{acc}$. The value $\dot{M}_{acc}\sim 10^{-10}$ M$_\odot$/y is a reasonable threshold for the transition from optically thick to optically thin (inner) disks (D'Alessio et al. 2006).

A last point to note is that disks with $\dot{M}_{acc}\gtrsim 10^{-9}$ M$_\odot$/y have all large excess emission (in the upper quartile of the distribution), and indeed the upper envelope of the $\dot{M}_{acc}$ distribution seems to correlate with the amount of excess emission. Given the small number of objects in the high range of $\dot{M}_{acc}$, the significance of this is unclear. If true, it would suggest a very interesting relation between $\dot{M}_{acc}$ and grain growth and settling, i.e., processes that can change the grain opacity and the disk flaring.

The potential of plots like Fig. 12 in constraining disk model parameters should be exploited further. However, this is well beyond the scope of this paper.

Fig. 12 also shows the location of the 11 EV disks with an $\dot{M}_{acc}$ determination. Nine of them have upper limits to $\dot{M}_{acc}$, some well below 10^{-10} M$_\odot$/y, and very small excess emission, generally below the lower quartile of the Class II distribution. From the upper limits to $\dot{M}_{acc}$, it is likely that at least half of them are indeed optically thin disks. There are two exceptions, one (SO908) is probably a missclassified Class II object, as it shows significant excess emission in all bands and broad Hα emission, consistent with its measured accretion rate ($\dot{M}_{acc}= 4\times10^{-10}$ M$_\odot$/y) (see Appendix C). The other EV object (SO1009) has one of the highest accretion rates in our sample (1.2×10^{-9} M$_\odot$/y) and no detectable excess emission in all bands; indeed, its classification as a disk object is dubious. No additional data are available in the literature, and we may have detected a strong chromospheric flare. It would be interesting to monitor this object further.

The location of the four TD on Fig. 12 is also shown. They are scattered through the plot: two (SO818 and SO897) are consistent (both in $\dot{M}_{acc}$ and excess emission, see also Appendix C) with optically thick inner disks. One (SO1268) has very likely a very optically thin inner disk, with a very low upper limit to $\dot{M}_{acc}(\sim 9\times10^{-12}$ M$_\odot$/y) and small excess emission even at 24 μm. The fourth TD object (SO299) has an accretion rate typical for its mass, 24 μm excess as Class II of similar accretion rate, but negligible excess in the IRAC bands. The large spread of properties of TD confirms the analysis of Muzerolle et al. (2010) and Sicilia-Aguilar et al. (2010) and their conclusions that very likely the "transitional" SEDs trace a variety of different physical situations.

7. Conclusions

We reported the results of a U-band survey with FORS1/VLT of a large area in the σ Ori star-forming region. We combined the U-band photometry with literature results to compute accretion luminosity and mass accretion rates from the U-band excess emission for all objects detected by *Spitzer* in the FORS1 field and classified by Hernandez et al. (2007) as likely members of the cluster. In total, there are 72 objects with evidence of a disk from near- and mid-IR photometry and 115 class III (diskless) stars. Among the disk objects, four (out of the seven identified by Hernandez et al. 2007) are transitional disks, and 14 are evolved disks. We derived the photospheric parameters of all stars from the existing V, R, I, and J photometry and used the U-λ colors of class III as templates for the photospheric and possible chromospheric emission. Our final sample, for which we provide estimates of the mass accretion rates, contains 58 Class II (49 class II stars for which we derive the accretion properties from the U-band excess emission, and nine stars with accretion properties from literature, for which we checked the consistency with our

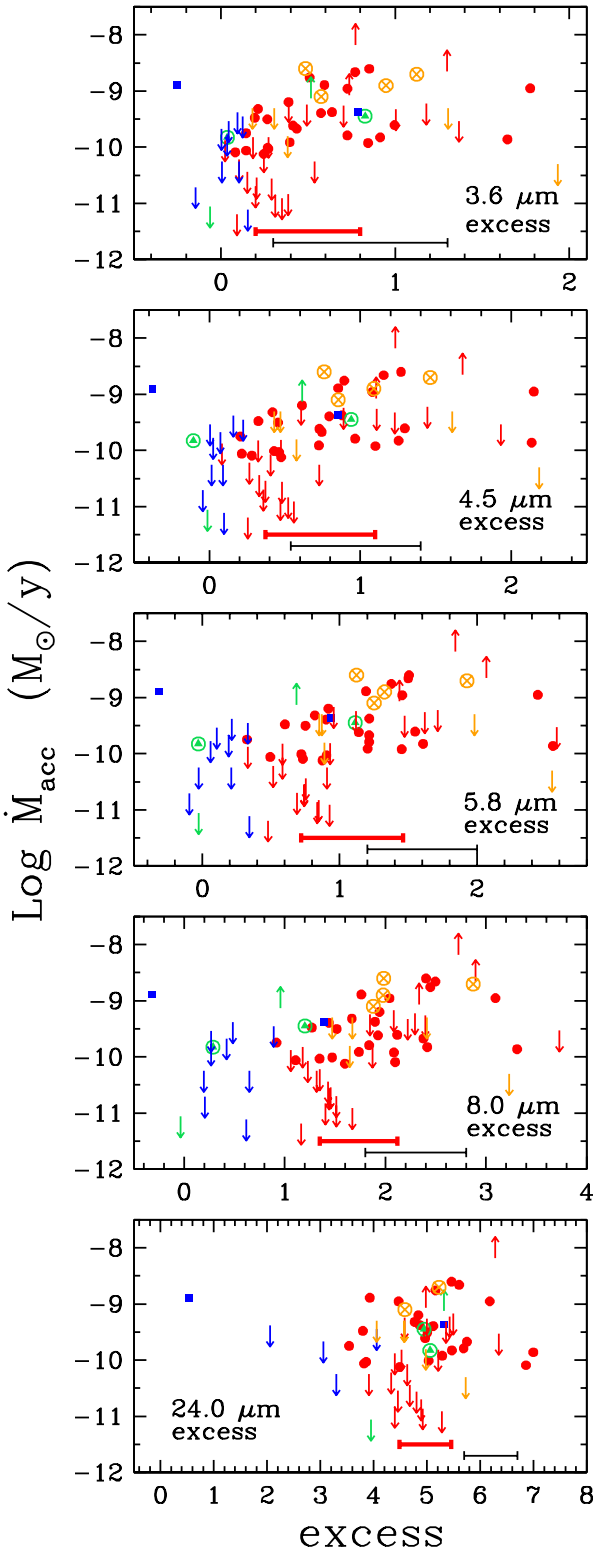

Fig. 12. $\dot{M}_{acc}$ vs excess emission (in mag) in the four IRAC *Spitzer* bands and for the 24μm MIPS band. The median excess emission and first quartiles are shown in each panel by the red (thick) horizontal lines; for comparison, we also plot the median Taurus class II SED (black (thin) line; D'Alessio et al. 2006). Symbols as in Fig. 7. (A color version of this figure is available in the online journal.)

results), four TD and 11 EV disks, over a mass range of between ~ 0.06 and $\sim 1.2 M_{\odot}$.

We analyzed the behavior of $\dot{M}_{acc}$ as function of mass and age of the individual stars, of the properties of the IR SED, and of the distance from the bright star σ Ori.

There is no correlation of $\dot{M}_{acc}$ with the distance from σ Ori, confirming that the effect of the O9.5 star on its surroundings is not strong (see also Hernandez et al. 2007); however, our sample does not include objects with projected distances smaller than 0.1 pc.

We find a strong relation between $\dot{M}_{acc}$ and M_*, with a very large spread of $\dot{M}_{acc}$ values for any given M_*, similar to other star-forming regions (Calvet et al. 2004; Natta et al. 2006; Fang et al. 2009; Sicilia-Aguilar et al. 2010). If fitted with a linear correlation, the slope is 1.6 ± 0.4. As noted by Vorobyov & Basu (2009) for a compilation of accretion rates in different star-forming regions, a linear fit is not the best description of the data. We computed median $\dot{M}_{acc}$ values and showed that the relation between $\dot{M}_{acc}$ and M_* is flatter at higher masses and steepens significantly for very low-mass stars and BDs. Such a trend is predicted by models of core collapse and disk evolution that include viscosity and gravitational instabilities (Vorobyov & Basu 2009), which control the evolution of more massive disks.

These models follow the disk evolution to the age of σ Ori, under the assumption that disks evolve only by accreting onto the star. However, other processes such as photoevaporation and/or planet formation, may cause disk dissipation (e.g. Hollenbach 2000; Dullemond et al. 2007). This may be a selective effect, which affects higher mass stars more than lower mass stars, changing the observed dependence of the $\dot{M}_{acc}$ distribution with M_*. We have compared the $\dot{M}_{acc}$–M_* distribution in σ Ori to that of the two other star-forming regions in the literature for which an IR-selected sample is available, namely ρ-Oph (Natta et al. 2006 and Appendix A) and Tr 37 (Sicilia-Aguilar et al. 2010). The comparison indicates that the median $\dot{M}_{acc}$ values for higher M_* are closer than predicted by simple viscous models, suggesting that selective disk dissipation may be important. However, we note that the significance of this comparison is not very strong, because the results for ρ-Oph are uncertain and the number of objects in each mass bin is not large. Moreover, the number and distribution of upper limits to $\dot{M}_{acc}$ affects the determination of median values in some mass ranges and prevents us from deriving upper and lower quartiles of the distributions.

The behavior of $\dot{M}_{acc}$ as function of the excess emission in the *Spitzer* bands suggests that at $\dot{M}_{acc} \sim 10^{-10}$ M$_{\odot}$/y the (inner) disks change from optically thin to optically thick. Objects with $\dot{M}_{acc}$ in the range $\sim 10^{-10} - 10^{-9}$ M$_{\odot}$/y span the whole range of observed excesses, from very low to very large. Objects with $\dot{M}_{acc} \gtrsim 10^{-9}$ M$_{\odot}$/y (the largest values in the sample) all have large IR excess. Viscous disk models (e.g., D'Alessio et al. 2006) predict that for $\dot{M}_{acc}=10^{-10}$ the surface density at 1 AU from a T Tauri star will be on the order of 1-10 g cm^{-2}, depending on the grain properties and dust settling. The emission of these disks in the *Spitzer* bands will be optically thin, unless grains are submicron size. The trend we tentatively observe among optically thin and optically thin disks, which needs to be confirmed in larger samples, may indicate a link between the mass accretion rate and the grain properties, which in turn control the disk geometry,a connection that is worth to be further explored.

The four TD stars included in our sample seem to cover a variety of properties, and only one of them has a mass accretion rate as Class II of similar mass, and negligible excess emission to wavelengths > 8μm. The other three could not be distinguished from Class II objects in the $\dot{M}_{acc}$ vs. excess emission plots. We can only agree with the conclusions that the "transitional" prop-

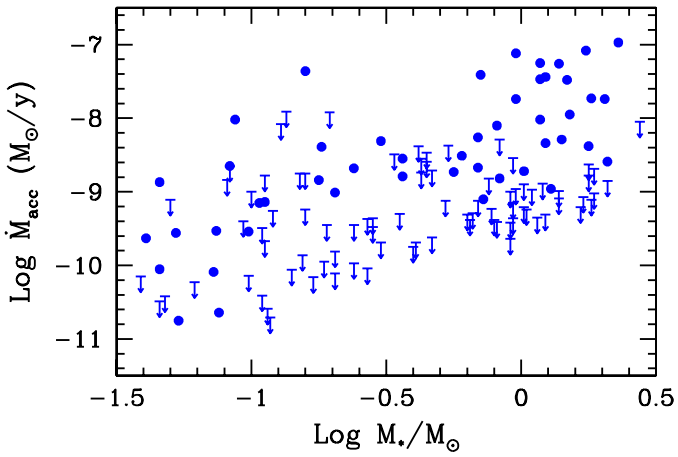

Fig. A.1. Mass accretion rate versus stellar masses for the star of the ρ-Oph sample. The stellar parameters and the accretion properties were recalculated assuming a distance of 130 pc (Lombardi et al.,2008) instead of 160 pc assumed by Natta et al. (2006), and 1 My age.

erties of the SEDs are likely caused by a variety of different properties (Muzerolle et al. 2010; Sicilia-Aguilar et al. 2010).

Acknowledgements. We thank Fabrizio Massi for useful suggestions on the data reduction and Nicolas Lodieu for providing the data on the σ Ori brown dwarfs. This publication is based on observations made with FORS1@VLT and SARG@TNG. We acknowledge the staff of the ESO Data Management and Operations department, who performed our observations in service mode.

Appendix A: ρ Ophiucus

The ρ-Oph sample is particularly interesting, because it is similar to the σ Ori one in being an IR-selected sample of class II, complete to a limiting mass of about 0.05 $M_\odot$ (Bontemps et al. 2001). Natta et al. (2006) computed mass accretion rates from the luminosity of Paβ assuming a distance of 160 pc; since no extensive spectral type determinations were available, they followed the method outlined by Bontemps et al. (2001) and derived the stellar parameters assuming coeval star formation at 0.5 My and the evolutionary tracks of D'Antona & Mazzitelli (1998; the isochrone method). They found that the mass accretion rates could be fitted by a linear relation $\propto M_*^{1.8\pm0.2}$ over a mass interval 0.03–3 $M_\odot$, with a very large spread for any given M_*. However, the Natta et al. (2006) results need to be reconsidered, since new measurements of the ρ-Oph distance yield considerably low values, 120-130 pc (Lombardi et al. 2008; Loinard et al. 2008; Snow et al. 2008). The corresponding decrease in luminosity implies an older age for the region. We have redetermined stellar parameters and mass accretion rates for all objects in Natta et al. (2006), adopting a distance of 130 pc and evolutionary tracks of Baraffe et al. (1998) for 1 My. The new values of $\dot{M}_{acc}$ are somewhat lower than previous ones, and M_* higher, especially for higher masses (see Fig. A.1).

As a consequence, if fitted with a single power-law, the correlation between $\dot{M}_{acc}$ and M_* is flatter, with a slope of 1.3 ± 0.2. The new distance, the older age and the different evolutionary tracks contribute to this result. In particular, the dependence of the $\dot{M}_{acc} - M_*$ relation on the adopted evolutionary tracks is well known (see Fang et al. 2009) and is particularly strong in ρ-Oph, given the method used to determine the stellar parameters.

Appendix B: BD and very low-mass stars from the Lodieu et al. photometric survey

An independent sample of very low-mass stars and brown dwarfs has been selected from the list of σ Ori members and candidate members of Lodieu et al. (2009). We applied a first selection criterium on the z,(z-J) diagram computed T_{eff} by comparing observed z, Y, J colors to synthetic ones from the theoretical models of Baraffe et al. (1998) for $\log g$=4.0 and luminosities from the observed J mag and model-predicted bolometric corrections. We then performed a further selection based on the location of the objects on the HR diagram, excluding all stars with M_*>0.13 $M_\odot$. Our sample of candidate young very low-mass stars and BDs in σ Ori is then formed by 80 objects, 40 of which were included in the U-band FORS1 survey.

Spitzer IRAC detections exist for 21/40 objects; three of them are uncertain members according to Hernandez et al. (2007). Of the 21, six are classified as class II, one is a transitional disk, one an evolved disk and 13 are class III objects. The 18 confirmed members are included in the sample analyzed in the main text of the paper. Note that the determination of the stellar parameters, T_{eff} in particular is performed using different photometric bands with respect to the bands used in the main text; the difference in T_{eff} are in general within the uncertainties discussed in §3.1; however, some of the objects in Table 2, although included in the Lodieu sample, were not selected with the criteria applied here.

Of the 40 objects in our sample, 20 have been detected in the U-band, while for the other 20 we have upper limits only. We derived the accretion luminosity and mass accretion rates as in §4.3. The calibration of the photospheric colors (U-J) and (U-I) as function of T_{eff} using our U-band photometry of Class III objects extends to $T_{eff}\sim$ 2900 K (Sec.4.1); we compare it to synthetic colors from the Baraffe et al. (1998) model atmosphere to extend the relations to lower T_{eff}. The Class III colors agree well with the models; the results are shown in Fig. B.1.

Fig. B.2 shows $\dot{M}_{acc}$ vs. M_*; we find that only five objects (all with M_* 0.06 $M_\odot$) have $\dot{M}_{acc}> -10.8$, the median in §6.1. of these, two are class II sources (SO500 and SO848, also in Table 2), one is a class III (SO641, possibly misclassified), three have no Spitzer detections. No other object with higher values of $\dot{M}_{acc}$ is detected.

Appendix C: SEDs and H_α of EV and TD objects

In this section, we show SEDs (Fig. C.1) and Hα profiles (Fig. C.2) of a subset of two TD and four EV stars observed with SARG@TNG (Sect. 2.4) and Giraffe (Sacco et al. 2008). A summary of the Hα properties is given in Table C.1, where 10% Hα represents the width of Hα at 10% of the line's peak intensity, and pEW is the pseudo-equivalent width. Below we will briefly comment on each object.

SO587. This EV disk was extensively studied by Rigliaco et al. (2009). It exhibits modest excess emission (well below the lower quartiles of the distributions) in the IRAC bands and at 24 μm. It shows a symmetric and narrow Hα emission profile with the peak close to the line center (type I profile following the classification of Reipurth et al. (1996)). Based on the available U-band photometry (Wolk 1996), the narrow Hα and the strength and profiles of the [S II] and [N II] forbidden lines, Rigliaco et al. (2009) suggested that the disk was being photoevaporated and that the forbidden lines were coming from the photoevaporation flow, possibly driven and certainly illuminated by the star σ Ori. A crucial ingredient of this model was the high ratio between the

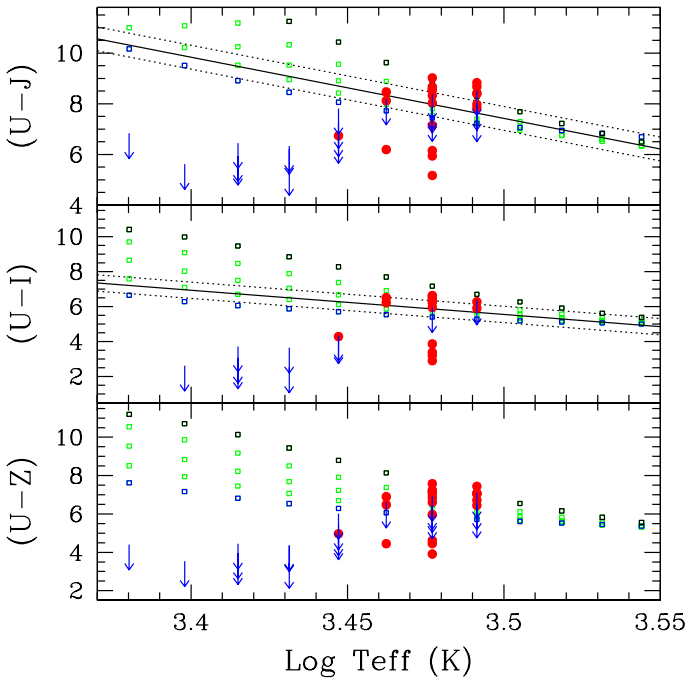

Fig. B.1. U-λ colors as function of T_{eff}. The red circles are objects with measured U-band fluxes, arrows are objects with U-band upper limits. The squares are model-predicted colors for different gravity, from 5.5 (black squares, top) to 3.5 (blue squares, lowest). The solid lines show the best-fit relations for Class III derived in Sec.4.1, extrapolated to lower T_{eff}; dashed lines are $\pm 2\sigma$. We will consider as accretors objects with colors below the photospheric strip: five BDs have clear evidence of U-band excess (note that for two we only have two colors), one only marginal evidence (from (U-I) and (U-J), while (U-Z) is photospheric). Hereafter we mark the upper limit as dashes for clarity. (A color version of this figure is available in the online journal.)

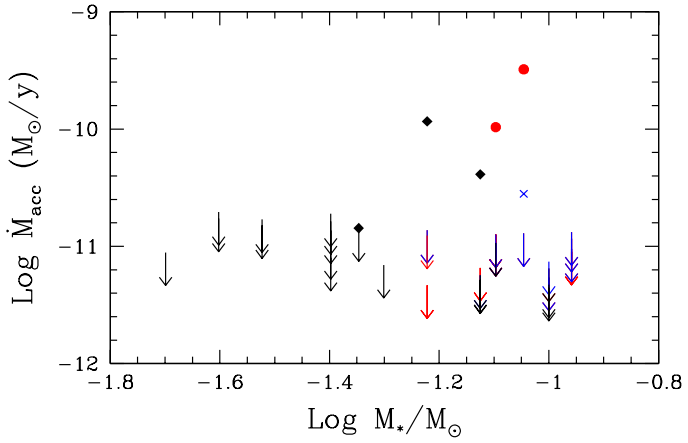

Fig. B.2. Mass accretion rate as function of M_*. Dots are class II objects with measured $\dot{M}_{acc}$, the cross is a class III stars with measured $\dot{M}_{acc}$, and diamonds refer to object with no *Spitzer* data. Arrows are objects with upper limits (both U-band detections and non-detections). Colors (only in the on-line version) indicate the SED Class : red for class II, blue for class III; black for objects with no *Spitzer* data. (A color version of this figure is available in the online journal.)

mass-loss and the mass-accretion rate. Our results confirm this interpretation. Although relatively bright in U, the object does not have a measurable U-band excess (i.e., it lies inside the photospheric strip of Fig. 4) and we estimate an upper limit to log $\dot{M}_{acc}$ of −9.45 $M_\odot$/y, consistent with the value −9.52 $M_\odot$/y derived in Rigliaco et al. (2009).

SO615. This is a relatively massive, luminous star. Its SED is typical of a flat disk up to 24 μm. We cannot measure $\dot{M}_{acc}$ from the U-band, which is already saturated by the photospheric emission alone, but we can estimate a value of log $\dot{M}_{acc}$ =−8.25 $M_\odot$/y from the U=15.96 mag measurement of Wolk (1996). The Hα has a complex profile, with broad wings, deep redshifted and blueshifted absorption and a narrow, slightly redshifted emission in the center. Similar profiles are observed for higher numbers of the Balmer series ("YY Orionis like profiles"; Walker, 1972) and are associated with extensive infall and outflow rates, consistent with the very high value of $\dot{M}_{acc}$. Unfortunately, the SARG SO615 spectrum is rather noisy.

SO759. Classified as EV disk star by Hernandez et al. (2007). The SED has negligible excess up to 8 μm, but a significant one at 24 μm, not very different from the SED of some TD objects. The Hα is rather narrow and symmetric, with a moderate red/blue asymmetry (type I profile, Reipurt et al. (1996)). The 10% Hα width of 157 ± 12 km s^{-1} and the upper limit log $\dot{M}_{acc}$ < −9.67 $M_\odot$/y is not stringent for an object of 0.3 $M_\odot$, but, combined with the Hα properties, it suggests that this is a low accretor (if any).

SO818. Classified as TD. This star shows significant excess emission, in the higher quartile at 3.6, 4.5, 5.8 and at 24 μm. We measure $\dot{M}_{acc}$=−9.45 $M_\odot$/y, typical of optically thick disks. The Hα is broad (10% width of 332 ± 25 km s^{-1}) and shows an inverse P-Cygni profile, with the emission peak at the line center position. The red-shifted absorption goes below the continuum (type IVR), confirming the evidence of a high accretion rate.

SO897. Classified as TD; the IRAC excess emission is clearly detected, but lower than the σ Ori medians, while the 24 μm excess is strong. We measure a lower limit to $\dot{M}_{acc}$(> −9.13 $M_\odot$/y), but the star is clearly accreting. We have two measurements of the Hα profile, one with Giraffe in October 2004 and one with SARG acquired in January 2009. Within these two epochs the maxima change in position and strength, with the primary one blue-shifted in 2004 and red-shifted in 2009, and the secondary one with opposite behaviour. The wavelength separation of the blue and red emission peaks decreases from 2004 and 2009, while the central reversal seems to be at the line center in the first epoch and then slightly blue-shifted in the second epoch. The profile changes from IIR to IIB, following the Reipurt et al. (1996) scheme, where these types are characterized by secondary peaks exceeding half the strength of the primary peaks, as we observe. This is a common phenomenon in accreting T Tauri stars, probably due to the interplay of variable accretion and mass-loss.

SO908. EV disk, with excess emission within the lower quartiles at all IRAC wavelengths, and significant excess at 24 μm. We measure $\dot{M}_{acc}$=-9.37 $M_\odot$/y, typical of optically thick disks. The Hα is broad and asymmetric, with less emission in the red than in the blue. This type of profile (IIIR) is the less frequent in the scheme classification of Reipurt et al. (1996). Following the radiative transfer models developed by Kurosawa et al. (2006), this profile morphology requires some obscuration by the dusty disk, i.e. a high inclination, explaining the rarity of the profile. A highly inclined disk is consistent with the SED properties.

Table C.1. Accretion properties of the stars shown in Fig. C.2. [a]Stars names, following the nomenclature of Hernandez et al. 2007; [b]values of the mass accretion rates derived from the U-band excess emission; [c]width of the Hα line at 10% of the peak; [d]values of the $\dot{M}_{acc}$ obtained using the empirical relation which involves the Hα width at 10% of the peak (Natta et al. 2004); [e]pseudo-equivalent width of the Hα line.

Object[a]	log M_{acc} ($M_\odot$/y)[b] (U-band)	10% Hα [c] (km s^{-1})	log M_{acc} ($M_\odot$/y)[d] (10% Hα)	pEW[e] (Å)	Instrument
SO587	< -9.45	191±10	-	-16.48±0.76	Giraffe
SO615	sat	397±50	-9.04	-4.4±0.4	Sarg
SO759	< -9.67	157±12	-	-3.39±0.22	Giraffe
SO818	-9.45	332±25	-9.67	-6.5±0.7	Sarg
SO897	> -9.13	235±19	-10.61	-4.21±2	Sarg
SO897	-	503±57	-8.0	-13.19±1.38	Giraffe
SO908	-9.37	401±26	-9.0	-19.65±0.19	Giraffe

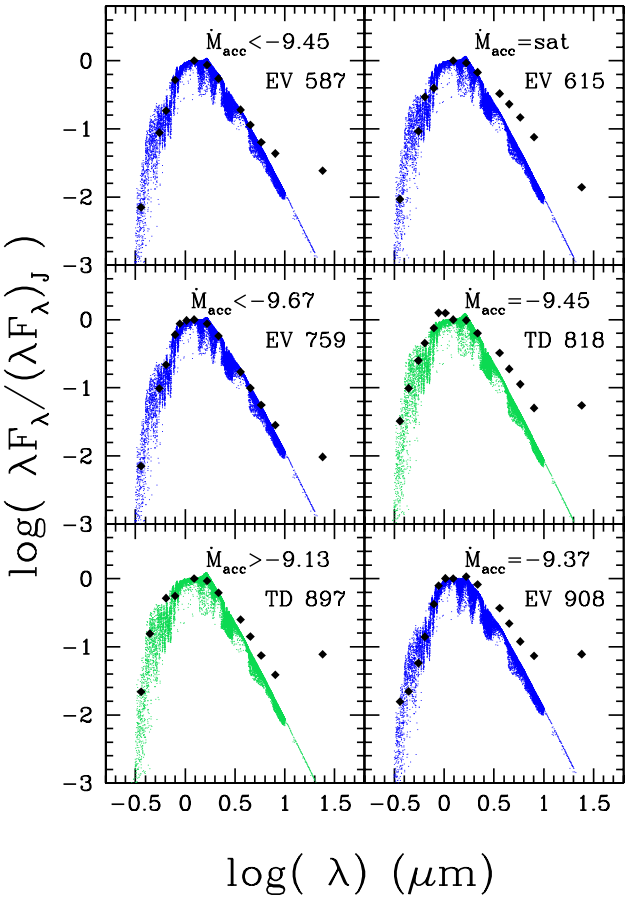

Fig. C.1. SEDs of four EV disks and 2 TD. The squares shows the observed fluxes (see Table C.2). The lines plot the model atmosphere from Allard et al. (2000) at the appropriate T_{eff}, $\log g = 4.0$, normalized to the J band. Each panel gives the name of the star (see Table C.1) and the mass accretion rate.

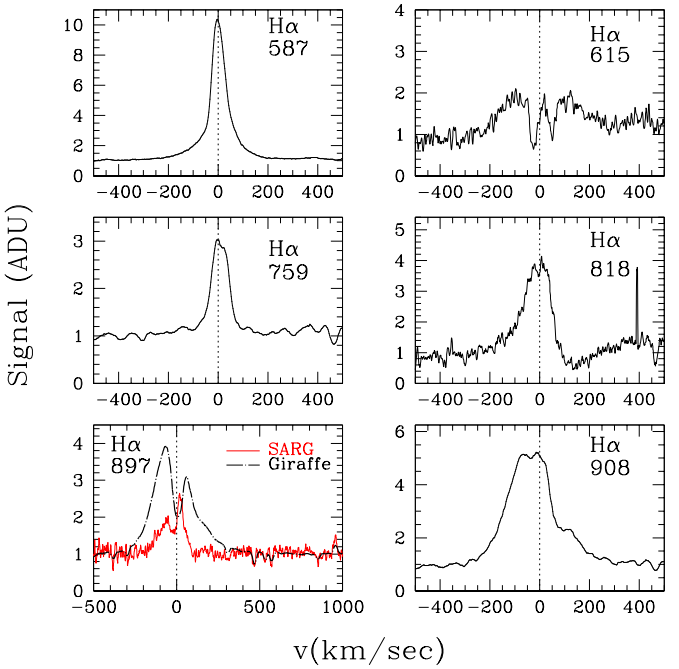

Fig. C.2. Hα line profiles of six stars of the sample normalized to the continuum. The spectra have been obtained either in 2004 with FLAMES/Giraffe by Sacco et al., with a spectral resolution R=17000, or by Rigliaco et al., in 2009 with SARG, with a spectral resolution R=29000, as indicated in Table C.1.

References

Béjar, V. J. S., Zapatero-Osorio M. R. & Rebolo R. 1999, ApJ, 521, 671
Béjar V. J. S., Martin, E. L., Zapatero Osorio, M. R., et al. 2001, ApJ, 556, 830
Baraffe, I., Chabrier, G., Allard, F., & Hauschildt, P. H. 1998, A&A 337, 403
Bontemps, S., André, P., Kaas, A. A., et al. 2001, A&A, 372, 173
Briceño, C., Vivas, A. K., Calvet, N., et al. 2001, Science, 291, 93
Brown, A. G. A., de Geus E. J., de Zeeuw P. T. 1994, A&A 289, 101
Caballero, J. A. 2007, A&A 466, 917
Calvet, N., D'Alessio, P., Hartmann, L., et al. 2002, ApJ, 568, 1008
Calvet, N., Muzerolle, J., Briceno, C., et al. 2004, AJ, 128, 1294
Calvet, N., D'Alessio, P., Watson, D. M. 2005, ApJ 630, L185
Clarke, C. J. 2007, 376, 1350
Currie, T., Lada, C., Plavchan, P., et al. 2009, ApJ 698, 1
Cutri, R. M., et al. 2003, 2MASS All Sky Catalog of Point Sources, The IRSA 2MASS All-Sky Point Source Catalog, NASA/IPAC Infrared Science Archive (Pasadena, CA: NASA/IPAC), http://irsa.ipac.caltech.edu/application/Gator
D'Alessio, P., Calvet, N., Hartmann, L., et al. 2006, ApJ, 638, 314
Dullemond, C., Natta, A. & Testi, L., 2006, ApJ, 645, L69
Dullemond, C. P., Hollenbach, D., Kamp, I., & D'Alessio, P., 2007, Protostars and Planets V, ed. B. Reipurth, D. Jewitt, & K. Keil (Tucson, AZ: Univ. Arizona Press), 783
Fang, M., van Boekel, R., Wang, W., et al. 2009, A&A, 504, 461
Feigelson, E. D. & Nelson, P. I. 1985, ApJ, 293, 192
Franciosini, E., Pallavicini, R., & Sanz-Forcada, J. 2006, A&A, 446, 501
Gomez de Castro, A.I., Franqueira, M., Huelamo, N. & Verdugo, E. 1998, Ap& SS, 261, 129
Gorti, U. & Hollenbach, D. 2009, ApJ 690, 1539
Gullbring E., Hartmann L., Briceño C. & Calvet N. 1998, ApJ, 492, 323
Jeffries, R. D., Maxted, P. F. L., Oliveira, J. M., & Naylor, T. 2006, MNRAS, 371, L10
Hartigan, P., Kenyon, S.J., Hartmann, L., et al. 1991, ApJ, 382, 617
Hartmann L., Calvet N., Gullbring E. & D'Alessio P. 1998, ApJ 495, 385

Hartmann, L., Megeath, S. T., Allen, L., et al. 2005, ApJ, 629, 881
Hartmann, L., Calvet, N., Gullbring, E., & D'Alessio, P., 2006, ApJ, 648, 484
Herczeg, G. & Hillenbrand, L. A. 2008, ApJ, 681, 594
Hernández, J., Hartmann, L., Megeath, S. T., et al. 2007, ApJ, 662, 1067
Hillenbrand, L. A. 2009, IAUS, 258, 81
Hollenbach, D., Yorke, H. & Johnstone, D. 2000, Protostars and Planets IV, ed V.Mannings, A. P. Boss & S. S. Russell (Tucson, AZ:Univ. Arizona Press), 401
Kenyon, S. J. & Hartmann, L. 1995, ApJS, 101, 117
Kenyon, M. J., Jeffries, R. D., Naylor, T., et al, 2005, 356, 89
Kurosawa, R., Harries, T. J.& Symington, N. H. 2006, MNRAS, 372, 1879
Landolt, A.U. 1992, AJ, 104, 340
Lodieu, N., Zapatero Osorio, M. R., Rebolo, R., et al. 2009, A&A , 505 1115
Loinard, L.; Torres, R. M.; Mioduszewski, A. J.; Rodrguez, L. F. 2008, IAUS, 248, 186L
Lombardi, M., Lada, C. J. & Alves, J. 2008 A&A, 480, 785
Luhman, K. L., Stauffer, J. R., Muench, A. A., et al. 2003, ApJ, 593, 1093
Muzerolle, J., Hillenbrand, L., Calvet, N., et al. 2003, ApJ, 592, 266
Muzerolle, J., Allen, L., Megeath, T., et al. 2010, ApJ, 708, 1107
Natta, A., Testi, L., Muzerolle, J., et al. 2004, A&A, 424, 603
Natta A., Testi L.& Randich S., 2006 A&A , 452, 245
Oliveira, J. M., Jeffries, R. D., & van Loon, J. T. 2004, MNRAS, 347, 1327
Oliveira, J.M., Jeffries, R. D., van Loon, J. T. et al. 2006, MNRAS, 369, 272
Perryman, M. A. C., Lindegren, L., Kovalevsky, J., et al. 1997, A&A, 323, L49
Persson, S.E., Murphy, D.C., Krzeminski, et al. 1998, AJ, 116, 2475
Rigliaco, E., Natta, A., Randich, S., Sacco, G. 2009, A&A, 495, L13
Reipurth, B., Pedrosa, A.; Lago, M. T. V. 1996, A&ASS, 120, 229
Sacco G., Franciosini E., Randich S., Pallavicini R. 2008, A&A, 488, 167
Sherry, W. H., Walter, F. M., & Wolk, S. J. 2004, AJ, 128, 2316
Sicilia-Aguilar, A., Hartmann, L., Szentgyorgyi, A., et al. 2005a, AJ, 129, 363
Sicilia-Aguilar, A., Hartmann, L., Hernández, J., et al. 2005b, AJ, 130, 188
Sicilia-Aguilar, A., Henning, Th. & Hartmann, L. 2010, AJ, 710, 597
Snow, T. P., Destree, J. D. & Welty, D. E., 2008, ApJ, 679, 512
Vorobyov, E.I. & Basu, S. 2009, MNRAS, 393, 822
Vorobyov, E.I. & Basu, S. 2008, ApJ, 676, 139
Walker, M. 1972, ApJ, 175, 89
Wolk, S. J. 1996, Ph.D. Thesis
Zapatero Osorio, M. R., Béjar, V. J. S., Pavlenko, Y., et al. 2002, A&A, 384, 937

Table C.2. U-band and collected literature photometry. The U-band magnitudes have been obtained with FORS1@VLT, the optical photometry is from Sherry et al. (2004), Kenyon et al. (2005), Zapatero-Osorio et al. (2002), Béjar et al. (2001) and Wolk (1996). JHK magnitudes are from the Two Micron All Sky Survey (2MASS) (Cutri et al. 2003). The magnitudes in the four channels of the Infrared Array Camera (IRAC; 3.8-8.0 μm) and the first channel of the Multiband Imaging Photometer for *Spitzer* (MIPS; 24 μm) are from Hernandez et al. (2007).

Name	RA (○)	DEC (○)	class	U (mag)	B (mag)	V (mag)	R (mag)	I (mag)	J (mag)	H (mag)	K (mag)	3.6 μm (mag)	4.5 μm (mag)	5.8 μm (mag)	8.0 μm (mag)	24.0 μm (mag)
SO209	84.46288	-2.43542	III	>23.0	...	...	...	17.135	14.921	14.374	13.954	13.64	13.53	13.68	13.38	...
SO251	84.47960	-2.46006	III	20.82	20.55	18.49	17.18	15.38	13.6	12.96	12.74	12.45	12.36	12.3	12.46	...
SO299	84.50394	-2.43548	TD	18.89	18.08	16.71	15.57	14.27	12.82	12.15	11.93	11.68	11.76	11.66	11.33	6.76
SO302	84.50689	-2.43130	III	19.82	18.71	17.21	16.01	14.54	13.03	12.32	12.07	11.86	11.83	11.78	11.8	...
SO320	84.51746	-2.31825	III	17.5	...	14.49	...	...	11.727	11.022	10.826	10.72	10.77	10.76	10.7	...
SO338	84.52699	-2.48038	III	<17	11.807	11.429	...	10.741	10.088	9.829	9.75	9.69	9.67	9.66	9.68	9.62
SO341	84.52801	-2.50627	II	18.07	16.46	15.08	14.08	13.14	11.76	10.92	10.54	9.73	9.47	9.2	8.43	5.4
SO352	84.53263	-2.52533	III	<17	...	...	...	...	10.566	9.93	9.769	9.63	9.65	9.58	9.56	9.54
SO366	84.53733	-2.33634	III	20.31	19.15	17.66	16.41	14.85	13.25	12.6	12.31	12.1	12.07	12.01	12.05	...
SO397	84.55490	-2.43573	II	18.69	18.41	16.92	15.67	14.1	12.48	11.82	11.55	11.16	10.96	10.66	9.98	7.68
SO426	84.56700	-2.63466	III	20.75	...	18.3	16.81	15.2	13.58	12.88	12.61	12.38	12.28	12.27	12.25	...
SO432	84.57150	-2.37377	III	21.92	...	19.08	17.3	15.25	13.61	13.03	12.74	12.33	12.26	12.21	12.17	...
SO435	84.57401	-2.68056	II	20.44	19.72	18.14	16.81	14.98	13.2	12.58	12.24	11.77	11.52	11.32	10.67	7.57
SO440	84.57490	-2.35288	III	17.07	...	14.43	13.32	12.53	11.77	11.09	10.88	10.81	10.89	10.86	10.78	...
SO444	84.57595	-2.80397	EV	19.23	18.14	16.68	15.54	14.15	12.76	12.02	11.8	11.62	11.57	11.51	11.29	...
SO460	84.58411	-2.63373	III	19.81	...	17.49	16.02	14.33	12.58	11.86	11.61	11.32	11.24	11.19	11.25	...
SO462	84.58536	-2.56910	II	19.32	18.94	17.29	16.07	14.36	12.65	11.92	11.65	11.03	10.63	10.14	8.97	5.9
SO465	84.58689	-2.77032	III	23.5	...	...	...	17.41	15.186	14.572	14.162	13.81	13.66	13.53	13.64	...
SO469	84.58898	-2.56002	III	>23	...	...	...	17.612	15.355	14.79	14.494	14	13.85	13.73	13.82	...
SO475	84.59063	-2.36375	III	<17	...	13.36	12.34	11.62	10.972	10.365	10.213	10.08	10.16	10.15	10.09	10.11
SO482	84.59605	-2.61371	II	19.94	...	18.66	17.14	15.67	13.8	13.17	12.78	12.22	11.8	11.3	10.76	...
SO485	84.59714	-2.42627	II	18.54	19.6	18.4	17.22	15.69	13.69	12.93	12.42	11.9	11.58	11.22	10.53	7.83
SO489	84.59799	-2.69212	III	20.74	...	18.26	16.84	15.08	13.29	12.74	12.4	12.16	12.04	11.98	11.99	...
SO490	84.59823	-2.34652	II	19.25	19.81	18.64	17.14	15.32	13.41	12.8	12.49	11.97	11.66	11.24	10.39	7.64
SO500	84.60588	-2.71143	II	20.73	...	...	...	17.3	14.88	14.16	13.57	12.75	12.37	12	11.37	8.59
SO502	84.60695	-2.52263	III	22.82	...	...	...	16.627	14.666	14.07	13.837	13.38	13.32	13.31	13.31	...
SO509	84.60924	-2.67810	III	23.37	...	...	...	17.283	14.909	14.281	13.918	13.55	13.48	13.45	13.46	...
SO514	84.61174	-2.64612	II	22.11	...	...	18.03	16.06	14.11	13.48	13.21	12.57	12.27	11.99	11.29	8.3
SO518	84.61349	-2.75263	II	<17	16.1	14.192	13.64	12.85	11.955	10.792	9.944	8.75	8.36	7.98	7.18	4.62
SO520	84.61455	-2.58446	II	19.23	...	17.09	15.84	14.38	12.83	12.11	11.86	11.43	11.16	10.68	9.73	6.62
SO521	84.61462	-2.72567	III	<16.5	10.9	10.8	11.2	10.396	10.176	10.099	10.103	10.04	10.04	10.05	10.05	9.61
SO525	84.61552	-2.71691	III	18.81	...	16.29	15	13.67	12.19	11.45	11.27	11.11	11.06	11.01	11.02	...
SO537	84.62065	-2.81309	II	>23.27	...	...	...	16.952	14.823	14.277	13.877	13.1	12.82	12.48	11.93	9.42
SO539	84.62125	-2.60070	III	19.01	...	16.34	15.22	14.04	12.63	11.89	11.69	11.53	11.52	11.49	11.46	...
SO540	84.62143	-2.27104	II	<17	15.4	14.49	13.2	12.954	11.697	11.021	10.759	10.51	10.41	10.26	9.42	4.99
SO545	84.62334	-2.42061	III	23.32	...	...	...	18.73	17.046	14.84	14.29	13.96	13.56	13.49	13.52	13.51
SO550	84.62529	-2.35547	III	17.19	...	14.81	13.73	12.96	12.2	11.55	11.39	11.28	11.35	11.33	11.27	...
SO557	84.62903	-2.56769	III	22.22	...	...	...	...	14.92	14.26	14.009	13.71	13.65	13.68	13.42	...
SO562	84.63079	-2.60936	II	16.98	16.64	16.3	15.09	13.78	12.174	11.473	10.986	10.32	9.88	9.51	8.5	5.57
SO563	84.63153	-2.58742	II	17.84	...	15.64	14.6	13.49	11.52	10.71	10.35	9.71	9.3	8.9	8.3	6.05

Table C.2. continued.

SO568	84.63512	-2.49917	III	>23	...	...	...	17.578	15.439	14.84	14.44	14.09	13.96	13.9	13.96	...
SO572	84.63676	-2.59419	III	17.04	...	...	13.71	12.739	11.544	10.896	10.73	10.57	10.54	10.57	10.53	...
SO576	84.63754	-2.65777	III	21.58	...	...	...	...	14.59	14.02	13.7	13.44	13.4	13.18	13.3	...
SO582	84.63890	-2.60486	III	18.64	...	15.87	15.51	13.39	12.052	11.295	11.107	10.95	10.94	10.91	10.91	...
SO583	84.64026	-2.73726	II	<16.5	13.5	13.6	...	11.509	10.131	9.28	8.666	7.68	7.37	7.02	6.05	2.95
SO587	84.64184	-2.61037	EV	18.83	...	16.39	15.24	13.72	11.98	11.33	11.08	10.73	10.56	10.43	9.86	6.92
SO590	84.64260	-2.57110	III	<16.5	8.543	8.556	...	8.57	8.779	8.82	8.79	8.84	8.8	8.76	8.8	8.65
SO592	84.64287	-2.58333	III	<17	...	...	...	...	11.22	10.56	10.35	10.26	10.36	10.22	10.23	...
SO598	84.64410	-2.68572	II	19.56	...	17.76	16.18	14.72	13.1	12.45	12.12	11.77	11.62	11.48	10.88	8.56
SO601	84.64494	-2.57098	III	<17	8.395	8.388	...	8.4	8.346	8.38	8.374	8.32	8.36	8.34	8.36	8.36
SO602	84.64509	-2.54782	III	<17	...	...	...	10.743	9.89	9.302	9.211	9.15	9.17	9.08	9.1	8.86
SO609	84.64726	-2.42280	III	>23.0	...	...	...	16.878	14.652	14.056	13.764	13.34	13.23	13.25	13.19	...
SO611	84.64769	-2.53098	III	16.67	...	...	13.24	12.501	11.303	10.627	10.46	10.34	10.33	10.28	10.23	...
SO615	84.64941	-2.73083	EV	<17	12.9	...	13.2	12.438	10.445	9.726	9.311	8.6	8.26	7.99	7.73	5.99
SO616	84.64942	-2.51199	III	16.52	17	13.701	13.28	12.48	11.245	10.598	10.424	10.32	10.29	10.24	10.21	...
SO620	84.65217	-2.55346	III	<16.5	7.77	7.88	...	7.99	8.1	8.18	8.202	8.22	8.28	8.2	8.26	7.75
SO621	84.65282	-2.73709	III	20.09	...	17.65	16.08	14.32	12.56	11.91	11.62	11.37	11.3	11.26	11.23	...
SO628	84.65598	-2.83985	III	20.28	19.33	17.85	16.43	14.66	12.81	12.18	11.92	11.62	11.55	11.55	11.51	...
SO631	84.65773	-2.34434	III	>23	...	...	19.55	18	15.6	14.92	14.64	14.14	14.04	14.01	14.36	...
SO638	84.66028	-2.58193	EV	<17	...	...	11.73	...	9.907	9.28	9.119	8.96	9.07	8.86	8.76	6.34
SO641	84.66072	-2.69883	III	21.65	...	...	18.28	16.36	14.56	13.97	13.65	13.31	13.25	13.16	13.2	...
SO644	84.66195	-2.46712	III	22.88	20.3	...	18.77	17.07	15.27	14.73	14.43	14.11	14.04	13.99	13.91	...
SO646	84.66254	-2.75888	II	17.66	...	17.26	15.92	14.58	12.91	12.2	11.89	11.19	10.86	10.5	9.92	7.98
SO648	84.66335	-2.88562	III	18.16	...	15.59	...	...	12.697	12.04	11.87	11.79	11.8	11.76	11.74	...
SO655	84.66545	-2.67210	III	20.68	...	...	...	...	13.75	13.1	12.88	12.55	12.48	12.48	12.49	...
SO657	84.66563	-2.53893	II	>23	...	...	...	17.556	14.89	14.284	13.942	13.18	12.82	12.44	11.7	8.61
SO658	84.66696	-2.84362	III	21.08	20.15	18.66	17.26	15.48	13.67	13.08	12.8	12.52	12.46	12.43	12.42	...
SO662	84.66770	-2.50515	II	17.22	15.98	14.27	13.74	12.89	11.51	10.76	10.4	9.84	9.42	8.88	8.08	5.51
SO663	84.66877	-2.55761	II	20.68	...	17.64	16.19	14.54	12.82	12.13	11.87	11.45	11.22	10.94	10.34	7.3
SO674	84.67322	-2.50798	II	19.52	...	17.04	15.84	14.39	12.84	12.14	11.93	11.69	11.56	11.29	10.55	7.44
SO692	84.68226	-2.87850	III	20.19	19.59	18.07	16.63	14.86	13.01	12.39	12.1	11.81	11.72	11.66	11.68	...
SO697	84.68423	-2.67209	II	16.71	...	...	...	12.51	11.36	10.69	10.44	9.83	9.41	8.90	7.81	5.20
SO700	84.68530	-2.67708	EV	>23	...	...	19.424	17.297	14.802	14.213	13.935	13.33	13.25	12.99	12.72	...
SO701	84.68532	-2.67507	III	20.28	...	...	...	14.99	13.37	12.72	12.5	12.24	12.22	12.24	12.23	...
SO710	84.68900	-2.69983	II	17.63	15.96	15.73	14.62	13.46	11.99	11.33	11.04	10.55	10.28	9.95	8.91	6.15
SO714	84.69149	-2.75640	III	20.97	...	19.15	...	15.49	13.56	12.96	12.69	12.34	12.27	12.24	12.26	...
SO728	84.69813	-2.45337	EV	19.69	...	...	...	14.05	12.14	11.5	11.27	10.91	10.86	10.74	10.57	...
SO730	84.69852	-2.51034	III	21.47	...	...	...	15.39	13.45	12.85	12.59	12.22	12.26	12.11	12.15	...
SO736	84.70019	-2.45398	II	<17	14.4	13.34	...	11.36	10.156	9.463	9.187	8.62	8.34	8.03	7.49	5.53
SO738	84.70032	-2.48150	II	22.4	...	...	...	16.44	14.47	13.84	13.44	13	12.72	12.37	11.55	8.58
SO739	84.70071	-2.73354	II	22.34	...	...	...	16.22	14.07	13.47	13.15	12.58	12.29	11.9	11.19	8.61
SO747	84.70481	-2.63955	III	<17	...	15.05	13.99	12.89	11.4	10.66	10.51	10.29	10.29	10.21	10.23	...
SO748	84.70501	-2.69025	III	18.45	...	15.98	14.73	13.23	11.7	11.01	10.7	10.57	10.53	10.54	10.49	...
SO750	84.70535	-2.39936	II	21.08	...	...	17.67	16.573	14.362	13.699	13.2	12.79	12.47	12.01	11.57	9.5
SO757	84.70797	-2.68965	III	19.33	...	16.97	15.58	14.21	12.77	12.03	11.8	11.58	11.56	11.55	11.53	...
SO759	84.70995	-2.44663	EV	19.35	...	16.79	15.58	14.1	12.5	11.84	11.54	11.37	11.23	11.09	10.85	8.44

Table C.2. continued.

SO762	84.71085	-2.71188	II	21.77	...	19.29	...	15.89	13.84	13.25	12.96	12.44	12.15	11.71	11.03	8.16
SO767	84.71257	-2.82059	III	22.81	...	...	...	16.9	15.04	14.42	14.16	13.79	13.71	13.56	13.74	...
SO774	84.71678	-2.77881	II	16.96	16.2	14.301	13.76	12.72	11.518	10.774	10.421	10.18	9.95	9.57	8.42	5.02
SO787	84.72228	-2.55633	III	<17	...	...	12.42	11.47	10.607	9.919	9.734	9.59	9.56	9.48	9.5	9.37
SO791	84.72552	-2.82499	III	<17	15	13.164	13.6	11.73	10.829	10.31	10.126	10.16	10.14	9.98	10.11	9.97
SO795	84.72658	-2.66761	III	21.91	...	19.11	...	...	14.311	13.698	13.381	13.04	13.03	12.97	12.92	...
SO797	84.72879	-2.48283	III	21.05	19.84	18.61	17.26	15.5	13.8	13.2	12.87	12.6	12.55	12.47	12.48	...
SO818	84.74306	-2.26953	TD	17.53	17.04	15.61	14.62	13.64	12.34	11.56	11.28	10.51	10.37	10.17	10.06	6.39
SO827	84.74685	-2.56428	II	18.96	18.24	17.14	16.09	14.83	12.888	11.979	11.401	10.87	10.47	10.09	9.27	6.42
SO841	84.75486	-2.61078	III	20.51	...	18.04	...	15.49	13.52	12.9	12.61	12.46	12.36	12.43	12.3	...
SO844	84.75575	-2.30771	II	16.97	16.28	15.01	14.02	12.99	11.73	10.84	10.34	8.93	8.52	8.2	7.53	4.55
SO847	84.75634	-2.64902	III	<16	7.97	8.06	...	8.21	8.131	8.105	8.093	8.07	8.06	8.06	8.06	7.73
SO848	84.75808	-2.58412	II	19.63	...	19.08	...	16.38	14.45	13.38	12.61	11.62	11.04	10.6	9.84	6.45
SO855	84.76159	-2.49887	III	19.6	18.42	16.91	15.72	14.21	12.61	12	11.69	11.47	11.39	11.35	11.37	...
SO859	84.76255	-2.69087	II	18.62	17.47	16.46	15.4	14.11	12.44	11.61	11.16	10.34	9.98	9.7	9.12	6.47
SO865	84.76500	-2.77413	II	18.54	18.04	16.94	15.82	14.37	12.84	12.12	11.86	11.47	11.22	10.9	10.12	6.83
SO866	84.76612	-2.33562	II	20.26	20.09	18.79	17.38	15.62	13.83	13.16	12.88	12.4	12.08	11.66	10.93	8.34
SO869	84.76859	-2.87525	III	17.17	...	14.54	...	...	11.66	10.988	10.814	10.7	10.68	10.59	10.63	...
SO877	84.77193	-2.55015	III	20.4	19.29	17.75	16.57	15.02	13.39	12.72	12.46	12.21	12.25	12.12	12.14	...
SO879	84.77262	-2.54176	III	17.06	14.7	14.44	13.53	12.83	11.55	10.86	10.67	10.58	10.66	10.59	10.55	...
SO896	84.78171	-2.47320	III	19.49	18.4	16.93	15.82	14.37	12.88	12.14	11.96	11.74	11.69	11.66	11.67	...
SO897	84.78176	-2.54423	TD	<17	15.5	...	13.44	12.921	11.298	10.573	10.26	9.75	9.65	9.58	9.31	4.98
SO902	84.78430	-2.54124	III	21.67	19.19	18.83	17.55	15.76	13.8	13.25	12.92	12.62	12.55	12.59	12.63	...
SO905	84.78563	-2.86296	EV	17.95	16.64	15.23	14.21	13.23	11.95	11.2	11.03	10.83	10.73	10.65	10.36	8.89
SO908	84.78665	-2.51992	EV	19.03	19.36	17.91	16.6	14.97	13.04	12.16	11.7	11.07	10.91	10.81	10.35	6.72
SO911	84.78742	-2.66611	III	22.76	...	...	...	17.37	14.66	14.13	13.74	13.26	13.16	13.26	13.12	...
SO917	84.79183	-2.46993	EV	21.52	...	...	17.68	16.05	14.6	13.99	13.78	13.56	13.37	13.4	13.09	...
SO924	84.79681	-2.43031	III	<16.5	...	15.32	...	...	10.963	10.593	10.475	9.62	9.03	8.35	7.18	4.64
SO925	84.79756	-2.55911	III	22.57	...	...	...	16.54	14.45	13.93	13.57	13.21	13.12	13.02	13.03	...
SO927	84.79804	-2.51851	II	18.14	16.31	15.32	14.4	13.45	11.99	11.19	10.73	9.62	9.03	8.35	7.18	4.64
SO929	84.79854	-2.60081	III	17.27	...	14.79	13.88	12.93	11.65	10.97	10.75	10.61	10.61	10.57	10.51	...
SO931	84.79945	-2.46140	III	20.63	19.64	18.03	16.84	15.2	13.61	12.98	12.65	12.52	12.39	12.39	12.29	...
SO933	84.80144	-2.50184	III	20.68	20.44	18.17	16.69	14.69	12.61	12.06	11.73	11.37	11.28	11.22	11.23	...
SO936	84.80457	-2.63085	II	>23.2	...	...	...	17.793	15.24	14.747	14.311	13.83	13.53	13.29	12.61	...
SO940	84.80616	-2.62760	III	20.91	...	18.33	...	15.65	13.41	12.77	12.5	12.21	12.15	12.1	12.04	...
SO946	84.81039	-2.47597	III	20.17	19.03	17.57	16.37	14.85	13.34	12.65	12.34	12.14	12.08	12.05	12.02	...
SO957	84.81302	-2.67986	III	23.26	...	...	...	17.279	14.669	14.042	13.656	13.31	13.21	13.11	13.14	...
SO961	84.81527	-2.49919	III	<17	...	...	...	...	9.808	9.498	9.398	9.4	9.37	9.33	9.32	9.38
SO967	84.81602	-2.61414	II	20.05	18.6	17.6	16.36	15.21	13.25	12.54	12.22	11.56	11.29	11.09	10.67	8.34
SO976	84.82092	-2.68808	III	21.27	19.6	18.6	...	16.31	14.29	13.63	13.37	13.1	13.03	13.01	12.97	...
SO978	84.82169	-2.42875	III	19.08	17.98	16.4	15.33	14.18	12.9	12.12	11.93	11.81	11.71	11.64	11.64	...
SO981	84.82534	-2.49126	EV	<17	...	...	...	11.729	10.721	10.27	10.117	10.08	10.04	9.98	9.98	8.64
SO984	84.82854	-2.51480	II	17.22	16	...	13.42	12.58	11.4	10.64	10.34	9.94	9.53	9.27	8.52	5.82
SO999	84.83439	-2.64050	III	21.41	21.12	18.97	17.57	15.56	13.61	13.04	12.78	12.49	12.32	12.27	12.26	...
SO1000	84.83535	-2.46025	III	18.55	17.43	15.93	14.81	13.52	12.15	11.43	11.17	10.98	10.94	10.89	10.89	...
SO1005	84.83749	-2.50929	III	21.34	19.7	...	17.9	15.74	13.29	12.75	12.44	12.09	11.97	11.93	11.82	...

Table C.2. continued.

SO1009	84.84067	-2.73437	EV	17.12	...	...	...	12.746	11.097	10.405	10.218	10.12	10.14	10.06	10.06	9.56
SO1017	84.84533	-2.55921	III	19.08	17.95	16.47	15.4	14.39	12.83	12.13	11.87	11.63	11.63	11.59	11.61	...
SO1027	84.85155	-2.56708	III	19.23	18.19	16.62	15.53	14.28	12.98	12.27	12.06	11.81	11.82	11.71	11.76	...
SO1036	84.85511	-2.63945	II	17.0	15.88	14.72	13.78	12.83	11.31	10.451	10.002	9.14	8.85	8.55	7.95	4.88
SO1037	84.85531	-2.46341	III	22.48	...	...	18.41	16.86	15.549	14.794	14.561	14.32	14.28	14.4	14.2	...
SO1043	84.85680	-2.56789	III	20.61	20.12	18.22	16.71	14.96	13.2	12.54	12.25	11.95	11.86	11.77	11.83	...
SO1050	84.85986	-2.47716	II	20.74	19.69	18.02	16.96	15.26	13.5	12.84	12.57	12.21	11.96	11.69	10.85	8.17
SO1052	84.86042	-2.43767	III	19.71	18.55	17.08	15.98	14.81	13.4	12.67	12.46	12.28	12.24	12.21	12.16	...
SO1053	84.86047	-2.87098	III	19.86	18.91	17.33	16.09	14.58	13.04	12.32	12.07	11.92	11.79	11.72	11.71	...
SO1057	84.86163	-2.71621	EV	20.77	21.49	18.9	17.25	15.52	13.18	12.4	12.12	11.85	11.76	11.62	11.18	8.88
SO1059	84.86194	-2.61567	II	>23.0	...	...	...	...	15.461	14.84	14.488	13.79	13.48	13.1	12.43	9.54
SO1075	84.87243	-2.45586	II	<16.79	...	...	...	14.81	12.84	12.02	11.46	10.74	10.28	9.67	8.79	5.56
SO1083	84.88062	-2.81475	III	20.39	19.72	18.18	16.86	15.2	13.616	12.933	12.665	12.45	12.38	12.29	12.4	...
SO1092	84.88490	-2.46588	III	16.56	...	...	...	12.682	11.175	10.498	10.326	10.21	10.27	10.23	10.18	10.12
SO1094	84.88578	-2.66231	III	<17	15.4	13.756	13.07	12.38	10.82	10.104	9.917	9.76	9.88	9.67	9.68	9.62
SO1097	84.88722	-2.79700	III	17.65	16.5	15.09	14.09	13.1	11.82	11.12	10.91	10.76	10.76	10.71	10.7	...
SO1104	84.89077	-2.34445	III	18.51	17.19	15.74	14.73	13.64	12.37	11.6	11.43	11.31	11.3	11.22	11.09	...
SO1108	84.89308	-2.64641	III	>23.0	...	...	...	17.48	14.763	14.188	13.787	13.39	13.27	13.25	13.1	...
SO1113	84.89641	-2.79165	III	16.65	...	...	...	...	11.775	11.069	10.953	10.79	10.82	10.81	10.75	...
SO1129	84.90363	-2.84027	III	<17	...	...	...	11.093	9.68	8.986	8.808	8.72	8.8	8.69	8.66	8.65
SO1133	84.90544	-2.44914	III	<17	16.25	14.84	13.89	12.98	11.698	10.974	10.773	10.66	10.65	10.61	10.58	...
SO1137	84.90753	-2.47907	III	16.66	...	...	...	...	11.319	10.671	10.554	10.42	10.39	10.38	10.35	...
SO1151	84.91396	-2.54043	III	21.29	20.35	18.78	17.34	15.52	13.44	12.9	12.53	12.23	12.14	12.14	12.14	...
SO1156	84.91740	-2.34667	II	<17	14.7	14.16	...	12.715	11.495	10.632	10.029	9.91	9.74	9.55	8.93	4.73
SO1162	84.91906	-2.65359	III	>23.0	...	...	18.89	17.293	15.4	14.669	14.408	14.13	14.03	14.02	14.1	...
SO1163	84.91906	-2.42975	III	<16	12	11.48	12.4	10.978	10.312	10.141	10.033	10.04	9.94	9.91	9.95	...
SO1182	84.92999	-2.54543	II	19.63	19.34	17.72	16.45	14.83	13.03	12.3	11.91	11.12	10.79	10.52	9.89	6.34
SO1186	84.93156	-2.77430	III	19.81	...	17.26	...	...	13.481	12.769	12.508	12.33	12.34	12.28	12.27	...
SO1193	84.93547	-2.41204	II	20.62	19.1	...	18.02	16.3	14.17	13.54	13.15	12.63	12.35	12.04	11.29	8.14
SO1204	84.94250	-2.67568	III	<16	9.08	9.01	...	8.94	8.876	8.894	8.8	8.89	8.86	8.82	8.85	8.84
SO1207	84.94425	-2.44208	III	20.45	19.65	18.05	16.65	14.87	12.99	12.36	12.05	11.77	11.64	11.65	11.69	...
SO1215	84.94760	-2.43790	III	<17	...	...	...	10.962	10.035	9.526	9.382	9.2	9.21	9.19	9.15	9.03
SO1216	84.94880	-2.60644	III	20.47	...	17.9	16.57	15.06	13.473	12.772	12.528	12.29	12.23	12.17	12.25	...
SO1217	84.94939	-2.54032	III	<17	...	...	...	...	10.969	10.287	10.082	10.05	9.98	9.93	9.93	...
SO1220	84.95028	-2.76591	III	19.31	18.1	16.58	15.49	14.18	12.92	12.28	12.03	11.82	11.81	11.72	11.8	...
SO1230	84.95609	-2.39614	II	20.02	20.21	18.15	16.86	15.12	13.4	12.76	12.44	12.07	11.91	11.61	10.99	8.58
SO1238	84.96074	-2.57051	III	20.97	19.4	18.43	17.9	15.52	13.68	13	12.73	12.47	12.5	12.38	12.39	...
SO1250	84.96875	-2.53406	III	<16.94	...	...	...	...	11.506	10.879	10.658	10.55	10.52	10.47	10.47	...
SO1260	84.97346	-2.56191	II	16.79	16.8	...	...	14.44	12.825	12.064	11.59	10.87	10.39	10.13	9.22	6.36
SO1266	84.97591	-2.45913	II	20.39	...	...	...	15.3	13.46	12.87	12.67	12.16	11.86	11.39	10.02	5.6
SO1268	84.97643	-2.62190	TD	>23.0	...	...	...	17.184	14.75	14.21	13.8	13.51	13.33	13.33	13.34	9.8
SO1269	84.97656	-2.74664	III	<17	...	...	...	11.484	10.133	9.491	9.293	9.17	9.27	9.13	9.12	9.18
SO1274	84.97777	-2.77618	II	<17	15.06	14.253	13.87	12.76	11.054	10.251	9.832	9.26	8.89	8.56	7.66	5.07
SO1275	84.97857	-2.32504	III	17.85	...	15.25	...	...	12.255	11.568	11.379	11.21	11.22	11.22	11.16	...
SO1282	84.98310	-2.34357	III	18.46	...	15.95	...	13.76	12.27	11.51	11.29	11.12	11.18	11.03	11	...
SO1295	84.98979	-2.53670	III	20.78	19.2	18.22	17.6	15.17	13.31	12.69	12.36	12.1	12.03	11.97	11.92	...

Table C.2. continued.

SO1296	84.99012	-2.79341	III	19.27	...	16.34	...	...	13.227	12.529	12.339	12.21	12.24	12.21	12.15	...
SO1323	85.00426	-2.33333	EV	20.82	...	18.45	...	15.31	13.1	12.5	12.25	11.91	11.81	11.83	11.6	...
SO1327	85.00816	-2.35904	II	18.58	...	16.84	...	14.06	12.34	11.58	11.25	10.64	10.35	10.22	9.67	6.22
SO1343	85.02133	-2.33315	III	17.34	17	14.493	14.22	12.95	11.46	10.77	10.542	10.4	10.39	10.36	10.33	...
SO1347	85.02210	-2.76069	III	<17	...	...	...	11.471	10.008	9.366	9.189	9.2	9.25	9.22	9.01	9.09
SO1353	85.02959	-2.54577	III	20.66	19	18.15	17.9	15.28	13.42	12.81	12.54	12.23	12.15	12.19	12.1	...
SO1359	85.03622	-2.54536	III	19.47	...	17.16	...	13.9	11.77	11.15	10.85	10.59	10.51	10.48	10.48	...
SO1361	85.03713	-2.55938	II	<17	16.2	15.1	...	13.907	11.501	10.546	9.911	9.1	8.72	8.33	7.5	...
SO1362	85.03891	-2.41853	II	19.8	...	18.27	...	15.15	13.15	12.5	12.15	11.51	11.09	10.66	9.87	...